minerals

MDPI

Article

Origin and Geodynamic Mechanism of the Tibetan Demingding Porphyry Mo (Cu) Deposit from Oceanic Subduction to Continental Collision

Yigan Lu [1,2,*], Kai Dong [1,*], Hui Zhou [3] and Zhuoyang Li [1]

[1] School of Natural Resources and Surveying, Nanning Normal University, Nanning 530001, China
[2] CAS Key Laboratory of Crust-Mantle Materials and Environments, School of Earth and Space Sciences, University of Science and Technology of China, Hefei 230026, China
[3] School of Civil and Architectural Engineering, Nanning University, Nanning 530001, China
* Correspondence: yglu210@ustc.edu.cn (Y.L.); dongkai@cug.edu.cn (K.D.)

Abstract: Demingding is a promising porphyry Mo-dominated deposit recently discovered in the eastern Gangdese metallogenic belt in Tibet, China. We present zircon U-Pb-Lu-Hf isotopic studies, as well as geochemical data of the late monzogranites and the prior rhyolites from the Demingding porphyry deposit to uncover their origin and geodynamic mechanism. Zircon U–Pb dating yielded precise crystallization ages of 17.3 ± 0.6 Ma (MSWD = 2.5) and 186.5 ± 3.0 Ma (MSWD = 2.0) for monzogranite and rhyolite, respectively. The monzogranite is characterized by high-K calc-alkaline, adakitic affinities, and positive zircon $\varepsilon_{Hf}(t)$ values (+0.9∼+5.6, avg.+3.1) with T_{DM2} (0.73–1.04 Ga), while the rhyolite has $\varepsilon_{Hf}(t)$ values of (+2.1∼+7.3, avg.+5.2) and T_{DM2} of (0.76–1.09 Ga) similar to the monzogranite. Our results suggest that the Demingding porphyry Mo (Cu) deposit is related to magma generated from the Neo-Tethyan oceanic subduction. The subsequent monzogranite porphyry was likely formed by the remelting of previously subduction-modified arc lithosphere, triggered by continental collision crustal thickening in Miocene. The lower positive $\varepsilon_{Hf}(t)$ values of monzogranites suggest minor inputs from the Mo-rich ancient crust, suggesting that Mo favors the silicate melt. Such magmatic events and special metallogenesis typify intracontinental processes and porphyry copper deposits, which are normally confined to oceanic subduction and Cu-dominated style, thereby making the continental setting and Mo-dominated style of Demingding exceptional and possibly unique.

Keywords: geochemistry; zircon U-Pb age; Hf isotope; Demingding porphyry deposit; Tibet

check for updates

Citation: Lu, Y.; Dong, K.; Zhou, H.; Li, Z. Origin and Geodynamic Mechanism of the Tibetan Demingding Porphyry Mo (Cu) Deposit from Oceanic Subduction to Continental Collision. *Minerals* **2022**, *12*, 1266. https://doi.org/10.3390/min12101266

Academic Editor: Michel Faure

Received: 4 September 2022
Accepted: 1 October 2022
Published: 8 October 2022

1. Introduction

The Tibetan Plateau is the best natural laboratory for studying dynamic processes of continental collision [1,2]. The associated Tethyan metallogenic belt is one of the most endowed metallogenic belts in China, which was formed in a continental collision setting [3–5]. Giant or large porphyry copper deposit (PCD) may not be solely produced by oceanic subduction [6–8], but might also be emplaced in the continental collision during the post-collisional extension of the intra-continental setting, which also favors large or even giant porphyry deposit [9–12]. Generally, in an arc setting, the porphyry Cu deposits are associated with a calc-alkaline suite whereas in the continental settings are associated with high-K to shoshonitic suites [13,14]. The Gangdese metallogenic belt is an important porphyry copper belt in the Tethyan metallogenic domain that host some famous large-size Cu (Au ± Mo) deposits, e.g., Qulong, Jiama, and Xiongcun, which were discovered over a decade [15–17]. Previous studies have shown that the host rocks of the aforementioned deposits are characterized by adakitic features [4,18,19]. Adakites are known to preserve the imprints of the lower crust, thus information regarding the nature of crust-mantle interaction and its implication on the metallogenesis in the region could be deciphered from the adakites in the Gangdese metallogenic belt (e.g., [14,18,20–23]). However, magmatism and mineralization associated with the transition between Pacific and Tethyan tectonic domains have not been well-elucidated, and the corresponding origins of the adakite in the Gangdese metallogenic belt are complex and remain enigmatic, thus hampering understanding of the regional geodynamic framework of the Gangdese belt and ore-forming processes.

Here, we present a detailed isotopic study of the recently discovered Demingding porphyry Mo (Cu) deposit, which is the eastern extension of the Gangdese metallogenic belt [24,25]. Consequently, the discovery of the Demingding porphyry Mo (Cu) deposit enriches the ore deposit association in the eastern part of the Gangdese PCDs metallogenic belt. Nevertheless, the Demingding Mo (Cu) deposit is poorly and least studied due to its high topographic altitude (ca. 5000∼5822 m) and harsh climatic conditions (snow cover almost year-round), which hampers the geological field mapping. In addition, the Demingding deposit is so unique, most of the Gangdese deposits are Cu-dominated whereas the Demingding deposit is Mo-dominated [25,26], which means this study will play a vital role in our understanding of the diverse nature and styles of the Gangdese metallogenic belt. In this study, we use Lu-Hf isotopes, together with whole-rock geochemistry and zircon U-Pb dating, which is newly designed to achieve the following goals: (1) to explore the origin and geodynamic mechanisms of the Demingding porphyry Mo (Cu) deposit in Tibet; and (2) to assess their significance in the understanding of the regional geodynamic setting and the mineralization styles of the Gangdese metallogenic belt.

2. Geologic Setting

2.1. Regional Geology

The Himalayan-Tibet plateau is the largest plateau on Earth, which is part of the Alps-Himalayan orogenic belt, formed due to the continental collision and subduction of India underneath Eurasia [27–29]. The Himalayan-Tibetan plateau consists primarily of four continental blocks, including the Himalaya, Lhasa, Qiangtang, and Songpan-Ganzi terranes, which are separated from south to north by the Indus-Yarlung Zangbo suture zone (IYZSZ), Jinsha suture zone (JSSZ), and Bangong-Nujiang suture zone (BNSZ), respectively (Figure 1a, [30]). The Lhasa terrane is divided into the northern Lhasa, central Lhasa, and southern Lhasa subterranes, which are separated from one another by the Shiquan River-Nam Tso Mélange Zone and the Luobadui-Milashan Fault. These subterranes are covered by different sedimentary and volcanic sequences [31,32]. In southern Tibet, the Lhasa terrane consists mainly of the Gangdese orogenic belt, which is regarded as a huge porphyry Cu-Mo-Au deposit belt.

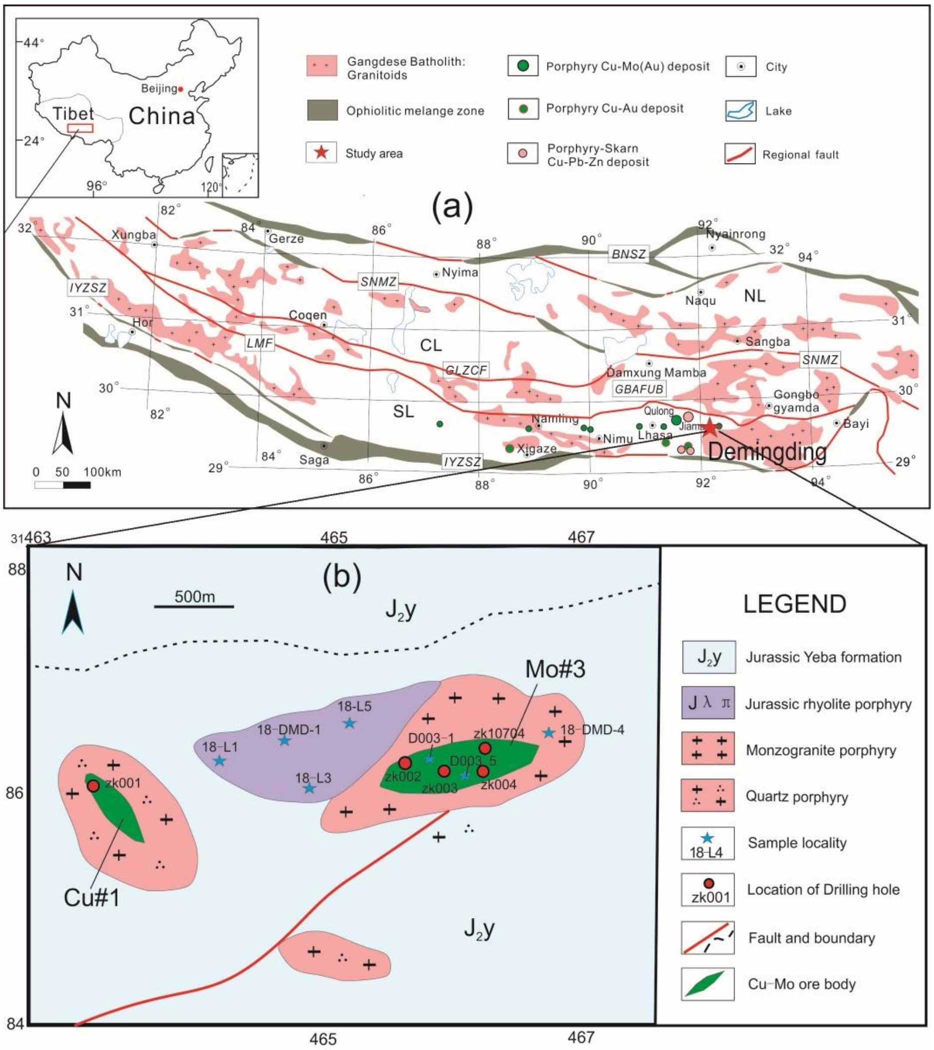

Figure 1. (**a**) Simplified geologic map of the Lhasa terrane showing the distribution of main porphyry deposits and locality of the study area (modified after [22,33]). Abbreviations: BNSZ = Bangong–Nujiang suture zone, SNMZ = Shiquan River-NamTso Mélange Zone, LMF = Luobadui-Milashan Fault, IYZSZ = Indus-Yarlung Zangbo Suture Zone, SL = southern Lhasa Terrane, CL = central Lhasa Terrane, NL = northern Lhasa Terrane. (**b**) Geological sketch map of the Demingding porphyry deposit showing the porphyry intrusion and locations of samples.

2.2. Geology of Ore Deposit and Sample Description

The Demingding porphyry Mo-Cu deposit is a promising deposit recently discovered in the eastern part of the Gangdese giant porphyry belt of Tibet (Figure 1b). The belt is one of the richest Cu provinces of the Tethyan-Himalayan metallogenic domain, hosting some of the largest PCDs in China (Figure 2a,b), and is widely accepted to represent a post-collisional tectonic environment [4,9,34]. Ongoing exploration and preliminary evaluations have estimated the Demingding porphyry deposit to be a medium to large-sized Mo-Cu deposit with inferred resources of >0.5 Mt Mo at 0.14% Mo and >0.5 Mt Cu at 0.26% Cu (Guangxi Nonferrous Metal Group Resource Exploration Co., Ltd., Nanning, China, 2017), mainly enriched in Mo (Figure 2c). The local geology is dominated by a volcano-sedimentary sequence including rhyolite and tuff of the Jurassic Yeba Formation [35]. At Demingding, the monzogranite porphyry represents the main ore-bearing intrusion (Mo#3), together with the earlier rhyolite porphyry, intruded into the Jurassic Yeba Formation (Figure 2a).

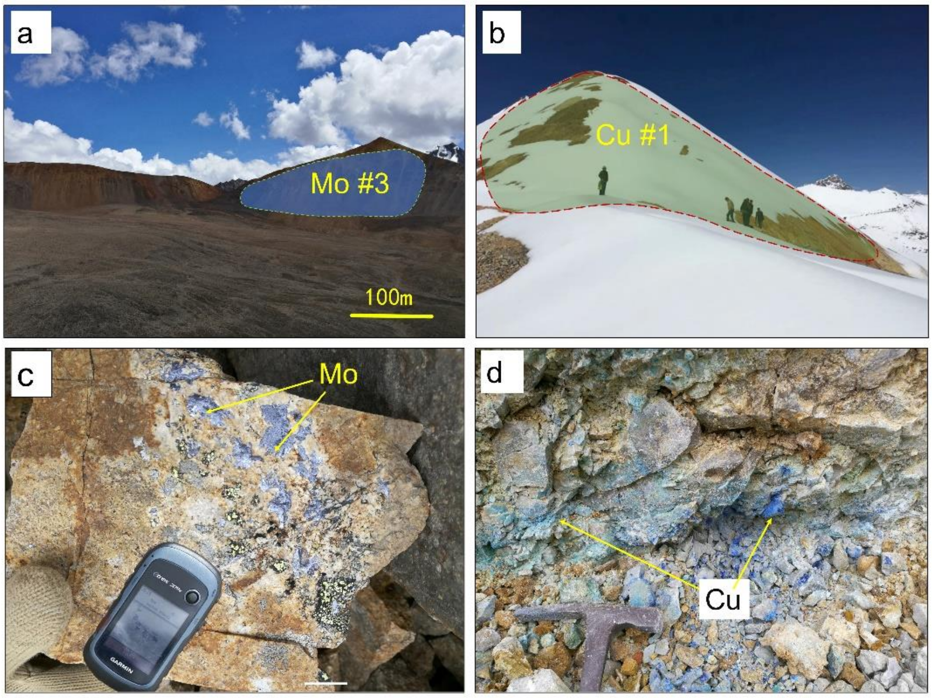

Figure 2. Photographs of the ore field and outcrops with Mo, Cu mineralization. (**a**) Locality of Mo#3; (**b**) Locality of Cu#1; (**c**) Molybdenum mineralization phenomenon; (**d**) Oxidized copper mineralization phenomenon. Abbreviations: Mo = molybdenite, Cu = copper-bearing minerals (e.g., malachite and azurite).

The monzogranite outcrop in the east-northern part of the deposit are characterized by a typical porphyritic texture comprised of phenocryst and matrix (Figure 3a). These rocks contain alkali feldspar (25%–30%), plagioclase (30%–35%), and quartz (20%–30%) with a minor amount of biotite (5%–10%) (Figure 3b). The accessory minerals are apatite, magnetite, zircon, and titanite.

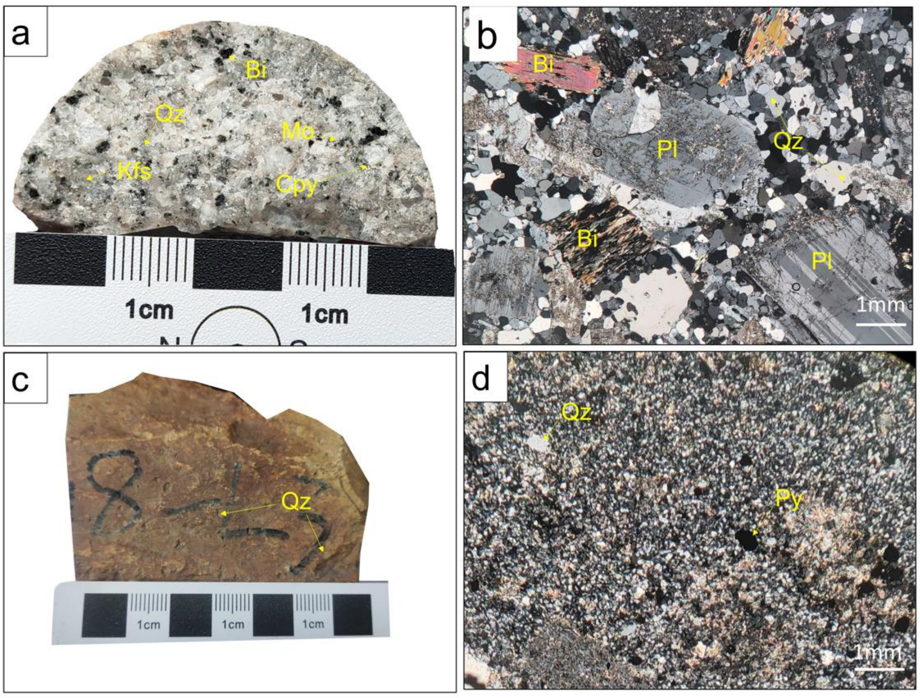

Figure 3. Photographs of representative rock samples of Demingding deposit and relevant photomicro

graphs: (**a**,**b**) Gray medium-grained monzogranite; (**c**,**d**) Beige or gray tiny-grained rhyolite. Abbreviations: Kfs—K-feldspar, Pl—plagioclase, Qtz—quartz, Bt—biotite; Py—pyrite; Cpy—chalcopyrite; Mo—molybdenite.

The rhyolite has a beige or gray color and contains phenocrysts of quartz and minor alkali feldspar, with a grain size of 1–2 mm (Figure 3c). The groundmass of rhyolites is quartz-feldspathic in nature and contain accessory minerals including zircon, titanite, and apatite.

The tuff has a tuffaceous texture and is mainly composed of rhyolitic tuff, 15%–25% crystal fragments, and minor lithic and plastic vitric fragment. Its crystal fragment comprises fine grain of quartz and feldspar, minor biotite (Figure 3d).

The mineralization-related monzogranite show concentric alteration zones including weak inner potassic alteration, phyllic zones characterized by replacement of plagioclase by quartz and sericite, and an outer prophylitic zone, and beyond that, kaolinitic alteration to ferroan carbonate alteration. Mineralization is characterized by disseminated chalcopyrite, pyrite, malachite, azurite, and molybdenite are mainly hosted within the potassic and phyllic zones.

A total of twenty fresh or minimally altered samples were obtained from the Demingding deposits, including nine samples from drill cores (ZK001, ZK002, ZK003, ZK004) and nine samples from field outcrops. Generally, the samples comprised of thirteen monzogranite samples and five rhyolite, which were subjected to geochemical analysis. Two samples (18-DMD-1 and 18-DMD-4) were selected for zircon U-Pb-Lu-Hf isotopic analysis.

3. Analytical Methods

3.1. Major and Trace Elements Analysis

A total of 18 samples from Demingding deposit were crushed and pulverized using an agate mill to ~200 mesh for bulk rock analyses (Processed by Yuheng Mineral and Rock Technology Company, Langfang City, China). After crushing, the samples were fused with Li tetraborate and Li metaborate in a ratio of 2:1 as fluxing and releasing agent, and the glasses were prepared by fusion in the ZSB0630 automatic electrofusion furnace. Major elements were analyzed using a Rigaku ZSX Primus II WDXRF X-ray fluorescence spectrometer at the University of Science and Technology of China, Hefei (USTC). Two standards (GSR-1 and GSR-9) were included as monitoring samples, with 2σ RSD of ±5%.

For trace elements, ~50 mg of powdered samples were dissolved in Teflon bombs for ~72 h in a mixture of HF-HNO_3 at 190 °C before evaporation. The dried samples were diluted to 80 g for analysis, following the procedures detailed by [36]. Trace elements were analyzed using an Elan 6100 DRC inductively coupled plasma mass spectrometer (ICP-MS) at USTC. The reference material BHVO-2 was used as standard to monitor the analytical quality with 2σ RSD of ±0.3%.

3.2. Laser Ablation ICP-MS Zircon U-Pb Dating

Zircon grains were separated from the rock samples, mounted in epoxy, and polished. Cathodoluminescence (CL) images were produced at USTC using a TESCAN MIRA 3 LMH FE-SEM and Gatan Chromal CL2 instrument. Zircons U-Pb isotopic ratios and trace element concentrations were measured using an Agilent 7700e ICP-MS attached to a Geolas 193 nm ArF-excimer laser at USTC. Spot size was set at 32 μm and a repetition rate of 10 Hz was used at 10 mJ. Ablated aerosols were transported to the ICPMS using He gas. The 91500 and NIST610 were chosen as standards for U-Pb dating and trace element analysis, respectively. The U-Pb ages and trace element contents were calculated using ICPMSDataCal software. The ^{29}Si was used as internal standard for concentrations [37,38].

3.3. Lu-Hf Isotopic Analyses

Hafnium isotopic ratios in zircon grains were measured using a Teledyne Cetac Technologies Analyte HE Excite 193 nm ArF laser-ablation system coupled to a Thermofisher

Neptune Plus MC-ICP-MS (LA-MC-ICP-MS) at the Isotope Laboratory of the School of Resources and Environmental Engineering, Hefei University of Technology (HUST). A fluence of ~6.0 J cm^{-2}, a repetition rate of 8 Hz, and a diameter of 55 μm was used to ablate the zircons for 30 s. Mixed He-Ar at a flow of ~0.9 L/min was used as carrier gas. Standard zircons (including Qinghu, Plešovice, Penglai, 91500, GJ-1) were used as quality control during the analytical process. All the data were reduced offline using LAZrnHf-Calculator@HFUT and the newly proposed isobaric correction model of [39]. Analytical results of standard zircons measured simultaneously are given and initial $^{176}Hf/^{177}Hf$ values were calculated based on a Lu decay constant of 1.865×10^{-11} [40]. The model ages were computed under the assumption that the $^{176}Lu/^{177}Hf$ of average crust is 0.015, and that the actual $^{176}Hf/^{177}Hf$ and $^{176}Lu/^{177}Hf$ ratios of chondrite and depleted mantle are 0.282772 and 0.0332, and 0.28325 and 0.0384, respectively [41].

4. Results

4.1. Major and Trace Elements

The result of whole-rock major and trace elements is presented in Table 1. The monzogranite samples show moderate to high silica contents (SiO_2 = 65.0~70.3 wt.%, avg. 68.3 wt.%, n = 13; Figure 4a); as such, the samples mainly fall in the field of granodiorite, while the rhyolites show high silica contents (SiO_2 = 67.4~74.9 wt.%, avg. 71.5 wt.%; n = 5), and as such span the fields of granite to granodiorite. Both the monzogranite and the rhyolite show relatively higher Al_2O_3 contents (12.3–15.5 wt.%) and as such span the fields of metaluminous and peraluminous in A/NK vs. A/CNK diagram (abbreviations: A—Al_2O_3, C—CaO, N—Na_2O, K—K_2O; Figure 4b). These rocks are mainly high-K calc-alkaline due to their high K_2O contents (3~4 wt.%) and K_2O/Na_2O ratio of about 0.9 (Figure 4c). All of the samples have low TiO_2 (0.3~0.4 wt.%) and MgO (0.4~1.3 wt.%) and Mg# values (31-51), and relatively lower CaO and Fe_2O_3 contents. Monzogranites are characterized by high Sr, high Sr/Y ratios (avg. 61), and low Y and Yb contents; whereas the rhyolites show lower Sr concentration, and higher Y and Yb contents. Most of monzogranite and rhyolite specimens are enriched in LILEs (e.g., Sr, Ba, K, Cs) and depleted in HFSEs (Nb, Ta, Ti) in trace element spidergram (Figure 5a), obviously enriched in LREE and relatively flat HREE pattern and negative Eu anomalies (Eu/Eu* = 0.6–1.0) in REE diagrams (Figure 5b).

Table 1. Major (wt.%) and trace element (ppm) concentrations of monzogranite and rhyolite samples from the Demingding deposit.

Sample No.	**18-L1**	**18-L2**	**18-L3**	**18-L4**	**18-L5**	**zk001-420**	**zk002-110**	**ZK002-210**	**zk003-51**	**zk003-120**	**ZK003-250**	**zk003-310**	**zk004-110**	**ZK004-258**	**D003-1**	**D003-2**	**D003-4**	**D003-5**
Rock Types			Rhyolite									Monzogranite						
Age (Ma)			186.5 ± 3.0									17.3 ± 0.6						
SiO_2	74.8	67.4	67.8	72.6	74.9	68.6	66.8	68.5	67.7	65.0	68.8	67.9	70.3	68.2	69.7	67.7	69.7	68.7
TiO_2	0.4	0.4	0.4	0.38	0.36	0.3	0.4	0.3	0.4	0.4	0.3	0.4	0.3	0.4	0.4	0.3	0.4	0.3
Al_2O_3	12.3	14.5	14.4	13.2	12.7	13.2	14.6	14.3	14.4	13.6	14.3	13.9	14.7	14.5	14.3	15.5	14.7	14.9
Fe_2O_3	3.6	3.1	3.1	2.3	1.9	3.1	2.5	2.1	3.4	3.6	1.9	2.6	2.4	2.5	2.0	2.1	1.3	2.3
MgO	0.9	1.3	0.9	0.6	0.44	0.6	0.9	0.8	1.1	1.2	0.7	1.1	0.7	0.9	1.1	0.9	0.8	0.6
MnO	0.10	0.11	0.12	0.08	0.10	0.02	0.04	0.05	0.03	0.05	0.03	0.04	0.04	0.04	0.04	0.03	0.03	0.05
CaO	3.9	2.1	3.1	2.4	1.36	1.6	2.2	2.6	2.4	2.9	2.0	2.1	2.6	2.4	2.4	2.3	2.1	1.3
Na_2O	1.1	4.2	3.6	3.4	4	3.4	4.5	4.5	3.9	3.9	3.8	3.4	3.9	4.8	3.9	4.6	4.1	3.4
K_2O	1.2	4.1	4.3	2.6	3.16	3.2	4.1	3.8	3.3	3.5	4.3	4.1	3.5	3.7	3.4	3.2	3.4	3.9
P_2O_5	0.09	0.13	0.13	0.08	0.05	0.10	0.14	0.14	0.19	0.18	0.12	0.16	0.14	0.15	0.14	0.14	0.16	0.13
LOI	2.3	2.8	2.7	3.1	1.08	4.5	2.6	2.5	2.3	4.2	3.0	2.9	1.0	1.9	1.3	1.8	2.1	2.5
Total	100.7	100.1	100.6	100.7	100.1	98.6	98.7	99.7	99.1	98.4	99.1	98.6	99.6	99.3	98.6	98.5	98.6	97.9
K_2O/Na_2O	1.09	0.98	1.19	0.76	0.79	0.95	0.91	0.84	0.85	0.89	1.11	1.18	0.91	0.78	0.86	0.70	0.84	1.15
Mg#	31.0	43.0	34.3	32.0	29.4	25.4	40.7	39.3	37.2	37.2	39.2	42.1	34.1	40.5	48.8	45.0	51.7	32.3
A/CNK	1.2	1.0	0.9	1.0	1.0	1.1	0.9	0.9	1.0	0.9	1.0	1.0	1.0	0.9	1.0	1.0	1.0	1.2
A/NK	4.0	1.3	1.4	1.6	1.3	1.5	1.2	1.2	1.4	1.3	1.3	1.4	1.4	1.2	1.4	1.4	1.4	1.5
Li	5.5	20.8	14.2	15.8	12.8	9.2	8.6	14.6	14.8	37.5	17.7	22.7	14.2	19.0	18.9	19.2	16.6	23.7
Be	0.8	1.8	1.6	1.2	0.9	0.8	2.0	1.8	2.2	1.9	1.7	2.2	2.5	2.0	2.0	2.2	2.1	2.0
Sc	12.0	8.0	6.7	6.4	7.0	11.6	5.7	6.1	6.6	7.0	7.6	6.3	5.6	6.3	4.0	4.0	3.8	4.6
V	67.0	58.0	48.0	26.0	22.0	133.9	44.1	37.4	56.2	54.9	46.1	47.2	40.1	46.7	41.2	39.5	36.8	35.7
Cr	14.0	18.0	9.0	5.6	5.4	40.1	13.9	7.6	12.9	7.9	6.8	8.0	6.4	7.8	147.6	107.3	109.6	100.6
Ni	7.0	11.0	5.0	4.5	2.3	33.0	7.4	7.8	11.2	9.4	9.1	8.6	5.3	7.3	72.9	54.8	53.3	51.8
Cu	11.0	20.0	7.0	2.5	4.5	118.1	107.0	135.1	313.0	52.0	420.0	166.8	68.5	1010.7	96.3	363.2	354.3	417.3
Zn	53.0	39.0	34.0	43.0	37.0	27.2	64.7	79.4	41.3	73.2	37.9	20.3	34.9	27.2	44.9	84.0	39.7	39.6
Ga	12.0	14.0	12.0	14.0	12.0	18.2	16.2	15.3	17.0	17.7	14.9	16.2	17.2	15.7	18.7	19.6	18.0	18.0
Rb	42.0	149.0	124.0	70.0	75.0	76.9	127.6	109.9	106.0	144.7	148.1	130.3	96.2	129.5	136.0	132.2	143.5	183.0
Sr	195.0	329.0	357.0	213.0	158.0	462.1	477.8	431.5	466.4	439.8	398.3	378.5	513.8	463.3	643.4	710.8	586.8	347.0
Y	30.0	19.0	18.0	28.0	36.0	12.9	8.3	8.3	11.6	8.5	11.4	8.5	7.1	9.7	5.6	7.3	7.8	7.8
Zr	117.0	152.0	146.0	177.0	262.0	131.6	75.9	52.6	59.0	54.4	57.1	60.8	51.6	37.8	38.6	37.7	39.3	31.2
Nb	3.2	12.0	10.0	9.0	12.0	2.9	8.8	8.4	13.4	9.6	11.0	10.0	8.1	12.8	7.4	6.8	9.3	5.6
Cs	5.4	7.3	1.1	4.1	4.2	2.1	3.1	2.1	6.5	10.8	7.0	11.4	5.2	7.2	3.2	9.4	10.5	9.9
Ba	267.0	625.0	576.0	421.0	708.0	515.5	836.3	541.0	459.8	711.8	560.6	773.9	515.6	1005.9	676.0	550.1	709.2	680.8
La	11.0	32.0	31.0	24.0	28.0	11.9	31.6	21.1	33.1	24.8	21.2	23.3	19.7	24.7	21.7	19.4	24.5	39.9

Table 1. *Cont.*

Sample No.	18-L1	18-L2	18-L3	18-L4	18-L5	zk001-420	zk002-110	ZK002-210	zk003-51	zk003-120	ZK003-250	zk003-310	zk004-110	ZK004-258	D003-1	D003-2	D003-4	D003-5
Ce	22.0	57.0	56.0	46.0	58.0	27.1	59.6	40.8	67.8	49.8	41.5	49.1	37.6	54.5	45.4	39.3	52.4	74.3
Pr	3.3	5.9	5.4	5.6	6.8	3.3	6.7	4.5	7.9	5.6	4.8	5.7	4.2	6.6	4.8	4.1	5.7	7.4
Nd	14.2	20.7	19.3	20.8	26.5	13.6	23.3	16.5	27.6	19.9	17.2	20.7	15.2	24.5	16.5	14.5	19.5	23.8
Sm	3.8	3.8	3.6	4.7	6.0	2.8	3.6	2.8	4.5	3.3	3.1	3.5	2.5	4.0	2.6	2.4	3.1	3.6
Eu	1.0	0.9	0.9	1.3	1.3	0.9	0.8	0.6	0.8	0.8	0.8	0.7	0.6	0.8	0.7	0.8	0.8	0.8
Gd	4.0	3.8	3.6	4.8	6.0	2.9	3.2	2.5	3.8	2.9	2.8	3.0	2.2	3.3	2.4	2.2	2.9	3.4
Tb	0.7	0.5	0.5	0.8	1.0	0.4	0.4	0.3	0.5	0.4	0.4	0.4	0.3	0.4	0.3	0.3	0.3	0.4
Dy	4.6	2.9	2.8	4.7	5.9	2.6	1.8	1.7	2.4	1.8	2.1	1.8	1.4	2.1	1.1	1.4	1.5	1.7
Ho	1.0	0.6	0.6	1.0	1.3	0.5	0.3	0.3	0.4	0.3	0.4	0.3	0.2	0.4	0.2	0.3	0.3	0.3
Er	3.0	1.9	1.7	3.1	3.8	1.5	0.9	0.9	1.2	0.9	1.2	0.9	0.8	1.1	0.6	0.7	0.8	0.8
Tm	0.5	0.3	0.3	0.5	0.6	0.2	0.1	0.1	0.2	0.1	0.2	0.1	0.1	0.2	0.1	0.1	0.1	0.1
Yb	3.2	2.0	1.9	3.3	4.0	1.4	0.8	0.8	1.2	0.8	1.3	0.9	0.8	1.0	0.5	0.7	0.7	0.7
Lu	0.5	0.3	0.3	0.5	0.6	0.2	0.1	0.1	0.2	0.1	0.2	0.1	0.1	0.2	0.1	0.1	0.1	0.1
Hf	3.1	3.2	3.1	4.3	6.3	3.6	2.4	4.2	2.1	1.9	2.0	2.5	2.0	1.4	1.4	1.4	1.4	1.2
Ta	0.2	0.7	0.6	0.6	0.7	0.3	0.7	0.7	1.2	0.8	1.1	0.9	0.7	1.0	0.7	0.6	0.8	0.5
Pb	11.4	14.1	9.6	13.7	13.2	4	94	62	31	121	51	29	27	31	37	42	37	45
Th	2.4	8.8	8.9	8.7	9.7	4	24	20	20	16	14	14	18	19	17	15	18	24
U	0.8	2.1	2.3	2.0	1.9	2.0	6.2	4.7	5.5	4.0	3.9	4.7	5.3	3.7	2.6	2.9	2.8	2.8
∑REE	103	152	146	149	186	82	141	101	163	120	109	119	93	133	103	94	120	165
Eu/Eu*	0.8	0.7	0.8	0.8	0.6	1.0	0.7	0.7	0.6	0.8	0.8	0.7	0.8	0.7	0.8	1.0	0.8	0.7

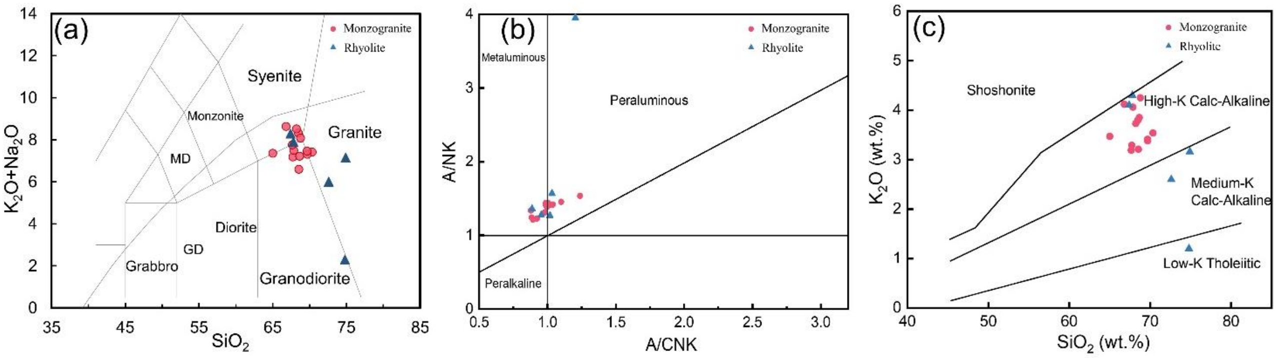

Figure 4. Geochemical features of the Demingding granitoid. (**a**) Diagrams of K_2O + Na_2O versus SiO_2, (**b**) A/CNK versus A/NK diagram, (**c**) SiO_2 versus K_2O plot. Abbreviations: MD—Monzodiorite; GD—Gabbro-diorite; A—Al_2O_3; C—CaO; N—Na_2O; K—K_2O.

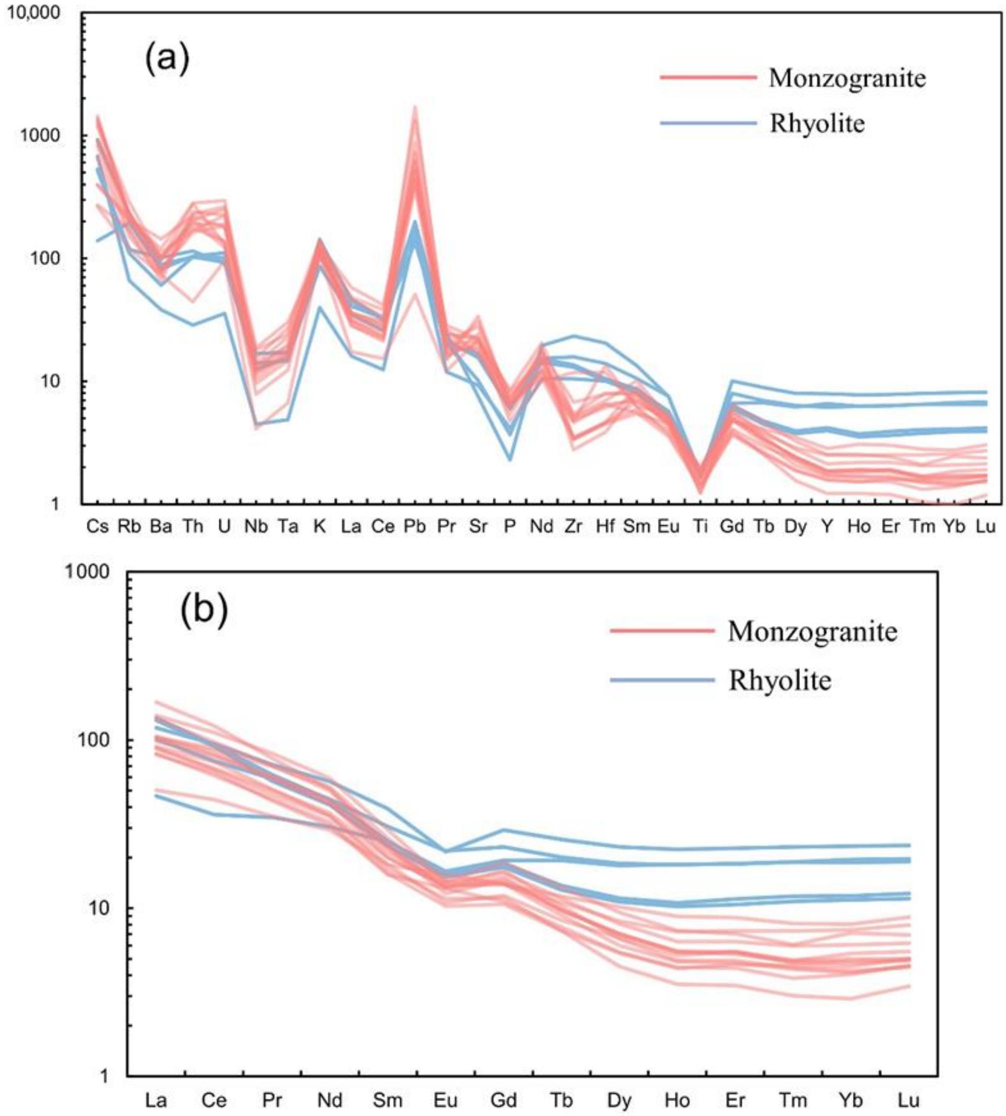

Figure 5. Primitive-mantle-normalized trace element (**a**) and chondrite-normalized REE (**b**) variation diagrams for samples from the Demingding deposit [42].

4.2. Zircon U-Pb Chronological Data

Zircon grains separated from Demingding monzogranites and rhyolites are generally prismatic, colorless, transparent, and euhedral. Cathodoluminescence (CL) images clearly show microscale oscillatory zoning, suggesting magmatic origin (Figure 6). The zircon data show concordant U-Pb data with weighted mean $^{206}Pb/^{238}U$ age of monzogranite porphyry that yielded an age of 17.3 ± 0.6 Ma (MSWD = 2.5, Figure 6a), suggesting that the Demingding monzogranite porphyry was formed in Miocene. The zircon grains from the rhyolite porphyry yielded a U-Pb age of 186.5 ± 3 Ma (MSWD = 2.0, Figure 6b), indicating the emplacing age of early Jurassic. Results of zircon U-Pb isotopic data are listed in Table 2.

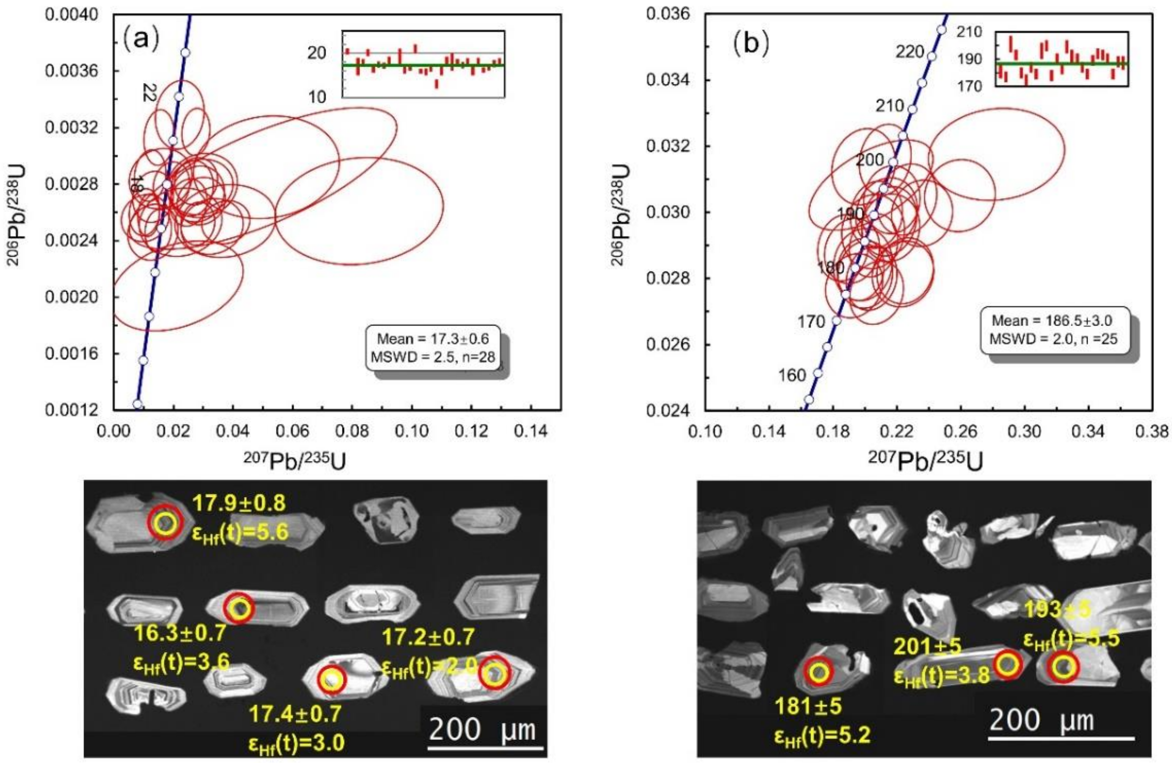

Figure 6. Zircon U-Pb Concordia diagrams and representative cathodoluminescence images, $^{206}Pb/^{238}U$ weighted ages and Hf isotopes of the monzogranites (**a**) and rhyolites (**b**) of the Demingding deposit. The small yellow circle represents the analysis point of zircon U-Pb age, while the large red circle represents the LA-MC-ICPMS in situ Hf isotope analysis point. The number next to the analysis point represents the U-Pb ages and the $\varepsilon_{Hf}(t)$ values.

Table 2. The results of Zircon U-Pb data of monzogranite and rhyolite samples from the Demingding deposit.

Measuring Point	^{232}Th $\times10^{-6}$	^{238}U $\times10^{-6}$	Pb* $\times10^{-6}$	Th/U	^{207}Pb/^{206}Pb Ratio	1σ	^{207}Pb/^{235}U Ratio	1σ	^{206}Pb/^{238}U Ratio	1σ	^{207}Pb/^{206}Pb Ma	1s	^{207}Pb/^{235}U Ma	1s	^{206}Pb/^{238}U Ma	1s
Sample. 18-DMD-4																
18-DMD-4-1	581.9	1024.1	4.1	0.6	0.06308	0.00731	0.02755	0.00314	0.00317	0.00011	711	266	28	3	20.4	0.7
18-DMD-4-2	308.3	182.7	0.8	1.7	0.22815	0.05398	0.08228	0.01862	0.00261	0.00025	3039	456	80	17	17.0	2.0
18-DMD-4-3	577.1	628.9	2.1	0.9	0.06861	0.01243	0.02625	0.00472	0.00277	0.00013	887	407	26	5	17.9	0.8
18-DMD-4-4	711.3	804.5	3.2	0.9	0.03523	0.00777	0.01519	0.00336	0.00313	0.00013	−64	304	15	3	20.1	0.8
18-DMD-4-5	649.3	654.7	2.4	1.0	0.10768	0.01547	0.03760	0.00533	0.00253	0.00010	1761	280	37	5	16.3	0.7
18-DMD-4-6	568.9	629.8	2.2	0.9	0.03529	0.01202	0.01319	0.00451	0.00271	0.00012	−62	480	13	5	17.4	0.7
18-DMD-4-7	740.5	860.4	2.9	0.9	0.06793	0.01134	0.02507	0.00416	0.00267	0.00011	866	362	25	4	17.2	0.7
18-DMD-4-8	475.0	492.4	1.7	1.0	0.04009	0.01767	0.01572	0.00696	0.00284	0.00014	−285	605	16	7	18.3	0.9
18-DMD-4-9	232.1	185.6	0.7	1.3	0.12697	0.04041	0.05119	0.01616	0.00292	0.00024	2056	681	51	16	19.0	2.0
18-DMD-4-10	497.3	558.9	1.8	0.9	0.09541	0.02006	0.03297	0.00689	0.00250	0.00013	1536	432	33	7	16.1	0.8
18-DMD-4-11	1209.5	1111.2	3.8	1.1	0.03285	0.00673	0.01167	0.00239	0.00258	0.00010	−162	248	12	2	16.6	0.6
18-DMD-4-12	444.4	548.0	2.2	0.8	0.04867	0.01186	0.02212	0.00539	0.00329	0.00016	132	410	22	5	21.0	1.0
18-DMD-4-13	1720.1	1121.3	4.0	1.5	0.04379	0.00867	0.01492	0.00296	0.00247	0.00010	−82	285	15	3	15.9	0.6
18-DMD-4-14	585.1	603.0	1.9	1.0	0.03868	0.01636	0.01312	0.00558	0.00246	0.00013	−368	611	13	6	15.8	0.8
18-DMD-4-15	1027.3	891.1	3.1	1.2	0.02996	0.01492	0.01058	0.00529	0.00256	0.00011	−286	577	11	5	16.5	0.7
18-DMD-4-16	246.8	314.9	1.1	0.8	0.07353	0.04934	0.02110	0.01471	0.00208	0.00021	1029	1205	21	15	13.0	1.0
18-DMD-4-17	430.8	483.5	1.6	0.9	0.06424	0.02618	0.02242	0.00917	0.00253	0.00016	749	794	23	9	16.0	1.0
18-DMD-4-18	1024.0	1154.5	4.2	0.9	0.03103	0.00885	0.01223	0.00350	0.00286	0.00012	−239	330	12	4	18.4	0.8
18-DMD-4-19	668.5	460.5	2.7	1.5	0.12796	0.06565	0.05011	0.02961	0.00284	0.00033	2070	1175	50	29	18.0	2.0
18-DMD-4-20	797.3	1004.0	3.4	0.8	0.05035	0.01055	0.01937	0.00406	0.00279	0.00011	211	373	19	4	18.0	0.7
18-DMD-4-21	983.2	1004.5	3.5	1.0	0.07935	0.01448	0.02935	0.00534	0.00268	0.00011	1181	373	29	5	17.3	0.7
18-DMD-4-22	966.3	673.9	2.6	1.4	0.07556	0.01875	0.02903	0.00720	0.00278	0.00013	1083	536	29	7	17.9	0.9
18-DMD-4-23	378.0	493.6	1.5	0.8	0.10690	0.03207	0.03746	0.01121	0.00254	0.00017	1747	597	37	11	16.0	1.0
18-DMD-4-24	408.6	460.4	1.6	0.9	0.07690	0.02023	0.02964	0.00779	0.00279	0.00015	1119	526	30	8	18.0	1.0
18-DMD-4-25	1650.8	1295.0	4.4	1.3	0.08118	0.01095	0.02820	0.00375	0.00252	0.00010	1226	247	28	4	16.2	0.6
18-DMD-4-26	906.9	909.7	3.1	1.0	0.02859	0.00938	0.01027	0.00339	0.00260	0.00011	−346	352	10	3	16.8	0.7
18-DMD-4-27	461.7	536.2	2.0	0.9	0.07470	0.01573	0.02818	0.00592	0.00273	0.00013	1060	417	28	6	17.6	0.8
18-DMD-4-28	697.2	705.9	2.5	1.0	0.07095	0.01230	0.02759	0.00476	0.00282	0.00011	956	338	28	5	18.1	0.7

Table 2. *Cont.*

Measuring Point	^{232}Th $\times 10^{-6}$	^{238}U $\times 10^{-6}$	Pb* $\times 10^{-6}$	Th/U	^{207}Pb/^{206}Pb Ratio	1σ	^{207}Pb/^{235}U Ratio	1σ	^{206}Pb/^{238}U Ratio	1σ	^{207}Pb/^{206}Pb Ma	1s	^{207}Pb/^{235}U Ma	1s	^{206}Pb/^{238}U Ma	1s
Sample. 18-DMD-1																
18-DMD-1-1	542.4	716.5	2.8	0.7	0.05064	0.00327	0.19871	0.01220	0.02842	0.00072	225	141	184	10	181	5
18-DMD-1-2	956.5	723.5	2.9	0.8	0.05039	0.00313	0.19330	0.01179	0.02778	0.00064	213	136	179	10	177	4
18-DMD-1-3	852.3	812.6	3.0	1.1	0.06443	0.00651	0.28244	0.02816	0.03175	0.00092	756	211	253	22	201	6
18-DMD-1-4	365.2	653.5	2.6	0.5	0.05172	0.00294	0.21693	0.01162	0.03038	0.00068	273	127	199	10	193	4
18-DMD-1-5	658.5	724.4	3.6	0.8	0.05053	0.00261	0.19727	0.00964	0.02827	0.00062	219	123	183	8	180	4
18-DMD-1-6	936.2	741.2	3.3	1.4	0.05447	0.00300	0.20739	0.01115	0.02757	0.00063	390	131	191	9	175	4
18-DMD-1-7	345.4	451.3	1.7	0.9	0.05127	0.00258	0.20531	0.01000	0.02900	0.00063	253	121	190	8	184	4
18-DMD-1-8	542.4	512.3	2.7	1.0	0.05155	0.00308	0.20018	0.01125	0.02812	0.00067	266	142	185	10	179	4
18-DMD-1-9	745.4	841.0	3.3	0.9	0.04798	0.00535	0.20392	0.02566	0.03082	0.00090	99	233	188	22	196	6
18-DMD-1-10	365.2	362.5	1.7	0.9	0.04874	0.00254	0.21264	0.01069	0.03159	0.00071	135	123	196	9	200	4
18-DMD-1-11	245.7	368.8	1.6	0.8	0.05279	0.00283	0.20419	0.01056	0.02801	0.00064	320	128	189	9	178	4
18-DMD-1-12	634.1	512.6	2.2	1.1	0.05159	0.00316	0.21359	0.01275	0.02998	0.00070	267	138	197	11	190	4
18-DMD-1-13	856.5	965.4	3.6	0.9	0.04822	0.00293	0.19195	0.01136	0.02883	0.00065	110	133	178	10	183	4
18-DMD-1-14	586.6	614.7	2.6	0.9	0.04595	0.00309	0.19910	0.01315	0.03138	0.00076	−5	144	184	11	199	5
18-DMD-1-15	489.8	612.7	2.7	0.8	0.04989	0.00357	0.20780	0.01392	0.03016	0.00075	190	158	192	12	192	5
18-DMD-1-16	425.3	452.3	2.0	0.9	0.05699	0.00323	0.23583	0.01264	0.02997	0.00066	491	124	215	10	190	4
18-DMD-1-17	912.4	1865.5	7.8	0.5	0.04664	0.00272	0.18624	0.01041	0.02892	0.00066	31	124	173	9	184	4
18-DMD-1-18	637.5	632.8	2.4	1.0	0.05775	0.00316	0.22511	0.01175	0.02823	0.00066	520	112	206	10	179	4
18-DMD-1-19	524.8	528.5	2.5	1.0	0.05240	0.00286	0.21516	0.01141	0.02973	0.00069	303	115	198	10	189	4
18-DMD-1-20	956.1	1002.5	4.7	0.9	0.06159	0.00371	0.25948	0.01466	0.03051	0.00072	660	120	234	12	194	4
18-DMD-1-21	425.4	415.7	3.0	0.9	0.05392	0.00303	0.22632	0.01242	0.03039	0.00071	368	118	207	10	193	4
18-DMD-1-22	714.4	745.8	3.4	0.9	0.05015	0.00275	0.20724	0.01076	0.02993	0.00067	202	116	191	9	190	4
18-DMD-1-23	301.4	354.2	1.2	0.7	0.05760	0.00343	0.22386	0.01274	0.02814	0.00066	515	129	205	11	179	4
18-DMD-1-24	635.7	765.3	3.1	0.9	0.05296	0.00312	0.21604	0.01200	0.02954	0.00067	327	131	199	10	188	4
18-DMD-1-25	398.7	534.6	2.2	0.8	0.05050	0.00336	0.20514	0.01296	0.02942	0.00074	218	147	189	11	187	5

4.3. Zircon Lu-Hf Isotopes

Zircon Lu-Hf isotopic results of the Demingding monzogranite and rhyolite samples are listed in Table 3. In this study, the Demingding monzogranites have ^{176}Hf/^{177}Hf ratios ranges from 0.282787 to 0.282920 (avg. 0.282850, n = 19), and ε_{Hf}(t) (t = 17.3 Ma) values from +0.9 to +5.7 (avg. +3.1, n = 19) with T_{DM2}(ca. 0.73–1.04 Ga). The rhyolites show a narrow range of ^{176}Hf/^{177}Hf ratios from 0.282729 to 0.282868 (avg.= 0.282814, n = 20), and ε_{Hf}(t) values from +2.1 to +7.3 (avg. +5.2, n = 20) with T_{DM2} (ca. 0.76–1.09 Ga).

Table 3. Hf isotopic compositions of samples from the Demingding deposit.

Sample No.	Rock Type	T (Ma)	^{176}Lu/^{177}Hf	2SE	^{176}Hf/^{177}Hf	2SE	$_{Hf}$(t)	2	T_{DM1}	T_{DM2}
18-DMD-4										
DMD-4-1		17.9	0.001021	0.000047	0.282919	0.000033	5.6	1.2	472.1	740.2
DMD-4-2		16.3	0.001268	0.000067	0.282863	0.000019	3.6	0.7	554.6	866.9
DMD-4-3		17.4	0.001504	0.000042	0.282847	0.000022	3.0	0.8	582.1	904.0
DMD-4-4		17.2	0.001052	0.000025	0.282818	0.000023	2.0	0.8	616.3	969.3
DMD-4-5		18.3	0.000963	0.000021	0.282823	0.000020	2.2	0.7	607.9	957.6
DMD-4-6		16.1	0.000899	0.000015	0.282787	0.000024	0.9	0.8	657.3	1039.2
DMD-4-7		16.6	0.001230	0.000019	0.282841	0.000019	2.8	0.7	586.8	918.4
DMD-4-8		15.9	0.000622	0.000052	0.282818	0.000018	2.0	0.6	609.3	969.7
DMD-4-9		15.8	0.000923	0.000033	0.282875	0.000018	4.0	0.6	533.4	841.2
DMD-4-10	monzogranites	16.5	0.000805	0.000015	0.282830	0.000018	2.4	0.6	594.7	941.4
DMD-4-11		16.0	0.000908	0.000033	0.282846	0.000022	3.0	0.8	573.8	905.8
DMD-4-12		18.4	0.001100	0.000065	0.282833	0.000017	2.5	0.6	595.6	934.6
DMD-4-13		18.0	0.001371	0.000054	0.282846	0.000020	3.0	0.7	581.1	905.3
DMD-4-14		18.0	0.000899	0.000021	0.282865	0.000018	3.7	0.6	547.4	862.8
DMD-4-15		17.3	0.000977	0.000025	0.282863	0.000019	3.6	0.7	551.6	868.1
DMD-4-16		17.9	0.000968	0.000051	0.282847	0.000020	3.0	0.7	573.9	903.5
DMD-4-17		16.8	0.001737	0.000068	0.282840	0.000022	2.7	0.8	596.4	921.0
DMD-4-18		17.6	0.001080	0.000054	0.282869	0.000024	3.8	0.8	543.9	853.4
DMD-4-19		18.1	0.001184	0.000021	0.282920	0.000020	5.6	0.7	472.2	737.2
18-DMD-1										
DMD-1-1		181	0.002336	0.000053	0.282815	0.000017	5.2	0.6	642.2	888.8
DMD-1-2		201	0.001919	0.000027	0.282762	0.000023	3.8	0.9	711.5	993.5
DMD-1-3	rhyolites	193	0.003611	0.000090	0.282820	0.000020	5.5	0.7	657.6	880.9
DMD-1-4		180	0.003450	0.000069	0.282831	0.000021	5.6	0.8	638.7	862.3
DMD-1-5		186	0.005190	0.000055	0.282788	0.000024	4.0	0.9	739.3	968.2

Table 3. *Cont.*

Sample No.	Rock Type	T (Ma)	$^{176}Lu/^{177}Hf$	2SE	$^{176}Hf/^{177}Hf$	2SE	$_{Hf}$(t)	2	T_{DM1}	T_{DM2}
DMD-1-6		184	0.004191	0.000167	0.282868	0.000019	6.9	0.7	594.7	781.9
DMD-1-7		179	0.004006	0.000050	0.282805	0.000023	4.6	0.8	689.1	925.7
DMD-1-8		200	0.004136	0.000135	0.282864	0.000022	7.1	0.8	600.3	783.7
DMD-1-9		190	0.002649	0.000012	0.282767	0.000023	3.7	0.8	718.5	994.1
DMD-1-10		186	0.003536	0.000058	0.282792	0.000025	4.4	0.9	699.0	947.2
DMD-1-11		192	0.002229	0.000068	0.282868	0.000027	7.3	1.0	563.3	763.5
DMD-1-12		184	0.003329	0.000130	0.282847	0.000020	6.3	0.7	612.4	823.4
DMD-1-13		186	0.003931	0.000083	0.282729	0.000026	2.1	0.9	803.2	1091.4
DMD-1-14		179	0.002909	0.000022	0.282850	0.000026	6.3	0.9	600.2	815.2
DMD-1-15		189	0.002336	0.000038	0.282829	0.000024	5.9	0.8	621.5	852.8
DMD-1-16		194	0.003380	0.000133	0.282822	0.000022	5.6	0.8	651.1	875.3
DMD-1-17		193	0.003244	0.000158	0.282794	0.000025	4.6	0.9	690.3	937.1
DMD-1-18		190	0.002401	0.000012	0.282832	0.000021	6.0	0.8	618.1	845.8
DMD-1-19		179	0.002214	0.000093	0.282810	0.000025	5.0	0.9	647.2	900.0
DMD-1-20		186	0.002101	0.000064	0.282796	0.000024	4.7	0.9	665.2	926.3

5. Discussion

5.1. Petrogenesis of the Ore-Bearing Monzogranites

Porphyry copper deposits typically occur in magmatic arcs settings above subduction zones and are genetically related to intermediate to felsic, hydrous calc-alkaline arc magmas that are predominantly formed by partial melting of the metasomatized asthenospheric mantle wedge [7,18,43]. However, recent studies have shown that porphyry Cu-Au deposits can also form in late-orogenic to post-collisional settings [4,14,16]. Generally, porphyry copper deposits are genetically associated with high Sr/Y or "adakitic" rocks [6,43,44]. Adakite is characterized by >56 wt.% SiO_2, $\geq$15 wt.% Al_2O_3 (rarely lower), mostly <3 wt.% MgO (rarely above 6 wt.% MgO), high Sr (mostly $\geq$ 400 ppm), and lower Y and HREE contents (e.g., Y and Yb lower than 18 and 1.9 ppm, respectively) than normal arc andesite-dacite-rhyolites (ADRs), low HFSE contents as in most island arc ADRs, and $^{87}Sr/^{87}Sr$ ratios usually $\leq$ 0.7040 [44,45].

The Demingding monzogranite varieties are characterized by high Sr (347~710 ppm) contents, low MgO (0.6~1.2 wt.%), high Sr/Y (35~116) and La/Yb (12~40) ratios, depleted in HREE (6~13 ppm) and Y (11~21 ppm), and slight negative Eu (avg. 0.8) anomaly, showing a typical adakite-like signature; whereas the rhyolites show normal arc andesite-dacite-rhyolite (ADRs) features (Table 1 and Figure 7), characterized by the continental marginal arc in petrological and geochronological characteristics. By contrast, the geochemical characteristics of monzogranite are also similar to the coeval intrusive rocks related to porphyry Cu deposits in the Gangdese metallogenic belt (e.g., [14,24,46–48]). Thus, the monzogranite might have a similar origin with the Miocene ore-bearing adakite-like porphyry varieties and the evolutionary process.

At least four genetic models have been proposed to account for the origin of Miocene adakite-like porphyry in the Eastern Gangdese metallogenic belt as follows: (1) Partial melting of the mantle wedge of the residual subducted Tethys oceanic plate [49–51]; (2) Magmatic mixing with felsic and basaltic magma [52–54]; (3) Partial melting of the lithospheric mantle peridotite [55,56]; (4) Partial melting of the thickened juvenile lower crust of Lhasa [4,57].

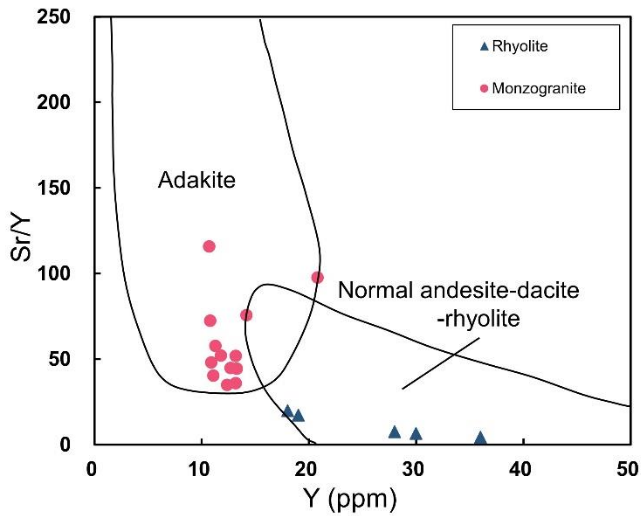

Figure 7. Sr/Y classification diagram for the Demingding monzogranite and rhyolite, after [45].

Among the above, Allègre and Minster [58] pointed out that the ratio of La, Nd, Th, Sm, Y, and other incompatible elements can effectively distinguish whether the rocks are formed by partial melting or differentiation and crystallization of magma. The ratio of Th, Nd, La, and other incompatible elements of monzogranites in the Demingding deposit show an obvious linear increasing trend on the partial melting evolution line (Figure 8), similar to adakitic rocks formed by partial melting such as the Qulong and Jiama deposits [59], indicating that partial melting occurred in the process of magma evolution rather than assimilation, or crystallization differentiation. In addition, Streck et al. [60] considered that adakitic rocks formed by magmatic mixing of felsic and basaltic melt usually contain high MgO content (>4.5%) and high Mg# (>66). However, the Demingding monzogranite samples are characterized by low MgO content (0.6%∼1.2%) and relatively low Mg# (32.3∼48.8). In the Mg# vs. MgO and SiO_2 diagrams, our samples were plotted in the field of origin from the lower crust (Figure 9). This is inconsistent with the characteristics of adakitic rocks formed by the mixing of felsic and basaltic magma. Moreover, the mantle peridotites are mainly composed of peridotite and pyroxenite melt, mainly forming basaltic magma rather than adakitic magma; hence, the Demingding monzogranites did not appear by partial melting of peridotite in the lithospheric mantle.

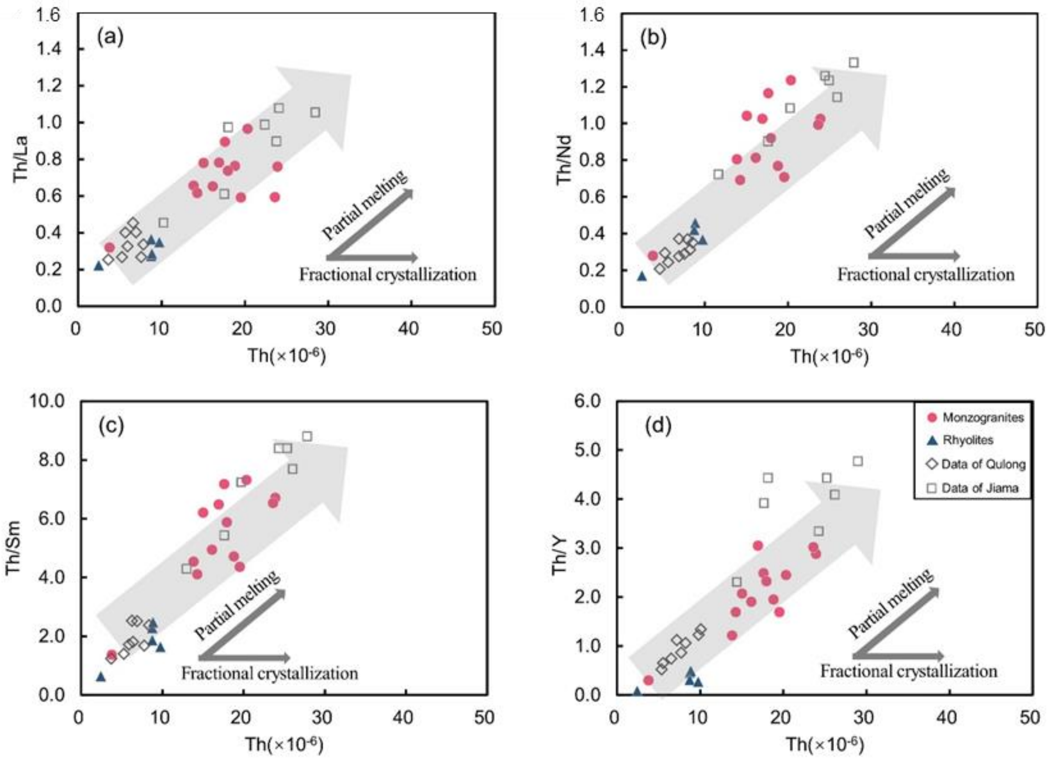

Figure 8. Correlation diagrams of Th/La (**a**), Th/Nd (**b**), Th/Sm (**c**), Th/Y (**d**) vs. Th for the Demingding monzogranites and rhyolites. Data sources: Qulong from [61]; Jiama from [62].

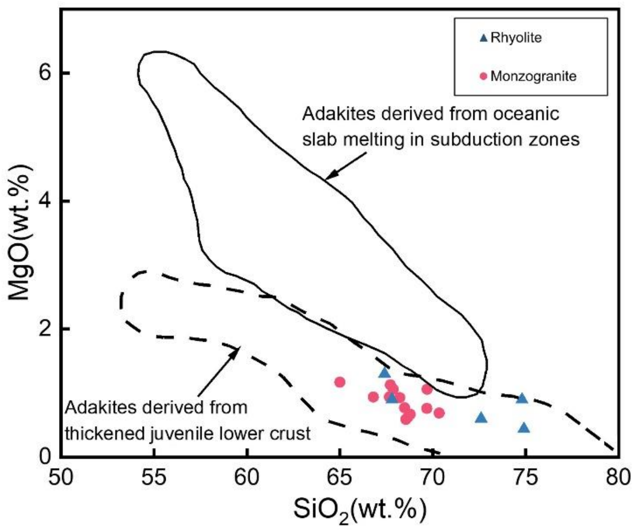

Figure 9. The plots of MgO versus SiO_2 field for the Demingding monzogranite and rhyolite, after [63].

Post-collisional magmatism can be considered as the second stage of melting of the subduction-modified upper lithosphere, which may remobilize metals and other elements accumulating during magmatism at the early stage [16]. In the Miocene period, the crust thickness of the Tibetan plateau increased to about 40∼55 km [1,64]. Studies have confirmed that the juvenile lower crust is mainly composed of eclogite and amphibolite facies that are rich in garnet when the crust attains a thickness of 40∼50 km [65]. Similarly, in the $(La/Yb)_N Yb_N$ diagram (Figure 10), the Demingding monzogranites plotted in the area of amphibolite facies to garnet-bearing facies (10%) indicate the existence of garnet-rich residual [66]. Experimental petrological studies have shown that the adakitic rocks formed by the partial melting of the thickened juvenile lower crust usually contain lower Mg# and

MgO, Cr, and Ni [67]. The accordance of low MgO content, low Mg# and low Cr, Ni and Co, high K_2O content, K_2O/Na_2O, Sr/Y, and $(La/Yb)_N$ ratio of the Demingding monzogranites, is also consistent with the petrogenesis and geodynamic setting of the Qulong intrusions in Miocene [68] and Jiru adakitic intrusions [59]. Particularly, the Gangdese adakitic intrusives have higher K_2O contents (3.2–4.3 wt.%), as partial melting of the mafic lower continental crust (LCC) under high pressure could produce high K_2O adakitic magmas with high K_2O/Na_2O ratios [69]. Therefore, we propose that the monzogranite were most likely formed by partial melting of the thickened juvenile lower crust [63].

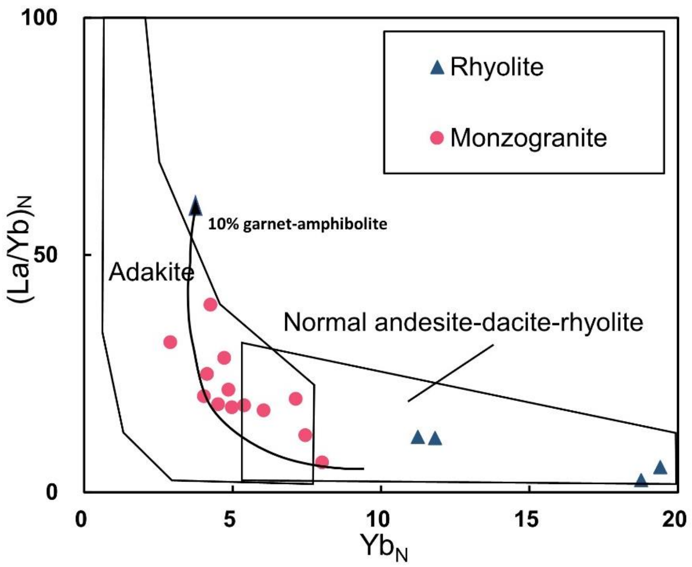

Figure 10. $(La/Yb)_N$ versus Yb_N classification diagram for the Demingding monzogranite and rhyolite, after [45].

5.2. Source Origin and Links between the Monzogranite Porphyry and Rhyolite Porphyry

Zircon Lu-Hf isotopes and their Hf model ages (T_{DMC}) can be used to distinguish juvenile mantle sources and give an estimated age when the magmatic source was extracted from a depleted mantle reservoir [49]. The Cenozoic collision-related Cu-Mo deposits in southern Lhasa subterrane are exclusively located in regions with high ε_{Hf} (>5) juvenile crust [4].

In the Demingding deposit, the positive zircon $\varepsilon_{Hf}(t)$ values (+0.9∼+5.6, avg. +3.1) with T_{DM2} (0.73–1.04 Ga) of monzogranites are slightly lower than the $\varepsilon_{Hf}(t)$ values of rhyolites (+2.1∼+7.3, avg.+5.2, T_{DM2} 0.76–1.09 Ga) in Mid-Jurassic Yeba formation (Table 3). These features are similar to other post-collisional porphyry intrusions such as Qulong (+6.2∼+9.9, avg.+7.8; n = 20; from [61]) and Jiama (+1.4∼+4.9, avg.+3.6; n = 14; from [62]) porphyry deposits in the Gangdese metallogenic belt. On the one hand, our samples plotted in the field between the mantle line and the chondrite evolution line, together with high Sr/Y ratios, show the characteristics of magmas derived at greater depth (Figure 11a). The $\varepsilon_{Hf}(t)$ values of monzogranites are on the normal evolution line of $\varepsilon_{Hf}(t)$ of rhyolites (Figure 11b), together with the identical ages of T_{DM1} and T_{DM2}, indicating that monzogranites and rhyolites likely have the same source region. The monzogranite is most probably derived from the thickened lower crust, which may have been accumulated by previous Neo-Tethyan oceanic subduction.

Post-collisional magmatism can be considered as the second stage of melting of the subduction-modified upper lithosphere, which may remobilize metals and other elements accumulating during magmatism at the early stage [16]. In the Miocene period, the crust thickness of the Tibetan plateau increased to about 40∼55 km [1,64]. Studies have confirmed that the juvenile lower crust is mainly composed of eclogite and amphibolite facies that are rich in garnet when the crust attains a thickness of 40∼50 km [65]. Similarly, in the $(La/Yb)_N Yb_N$ diagram (Figure 10), the Demingding monzogranites plotted in the area of amphibolite facies to garnet-bearing facies (10%) indicate the existence of garnet-rich residual [66]. Experimental petrological studies have shown that the adakitic rocks formed by the partial melting of the thickened juvenile lower crust usually contain lower Mg# and MgO, Cr, and Ni [67]. The accordance of low MgO content, low Mg# and low Cr, Ni and Co, high K_2O content, K_2O/Na_2O, Sr/Y, and $(La/Yb)_N$ ratio of the Demingding monzogranites, is also consistent with the petrogenesis and geodynamic setting of the Qulong intrusions in Miocene [68] and Jiru adakitic intrusions [59]. Particularly, the Gangdese adakitic intrusives have higher K_2O contents (3.2–4.3 wt.%), as partial melting of the mafic lower continental crust (LCC) under high pressure could produce high K_2O adakitic magmas with high K_2O/Na_2O ratios [69]. Therefore, we propose that the monzogranite were most likely formed by partial melting of the thickened juvenile lower crust [63].

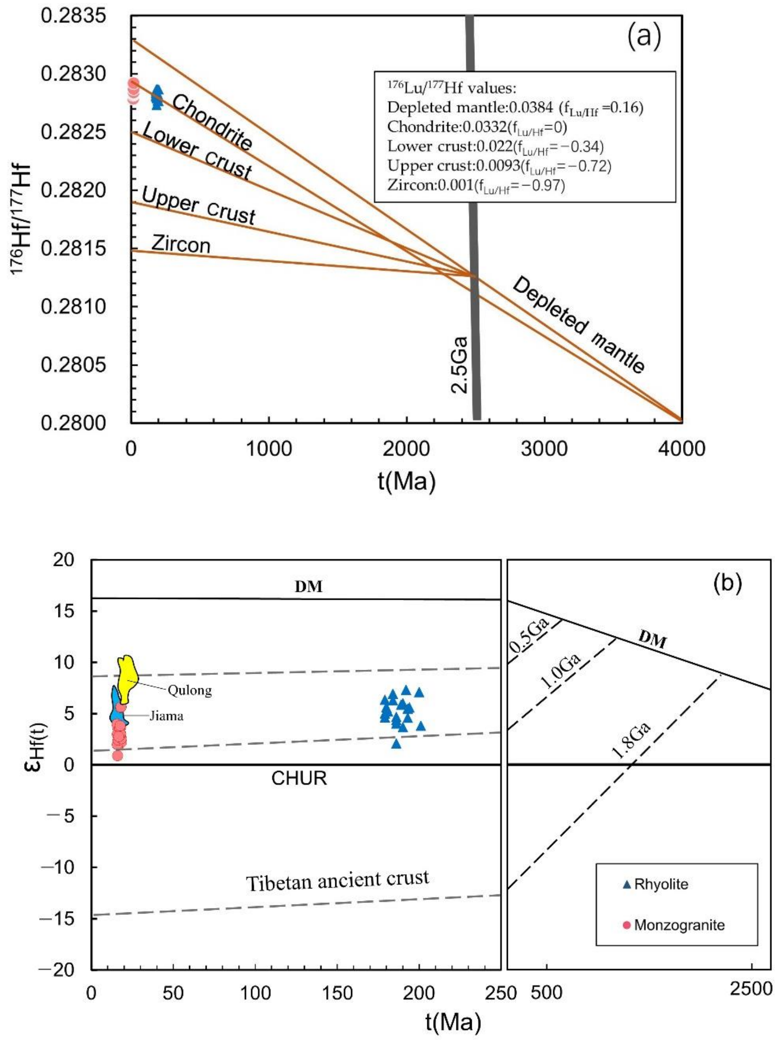

Figure 11. Zircon $\varepsilon_{Hf}(t)$ data plotted against zircon U–Pb ages. Data sources: Qulong from [61]; Jiama from [62]. DM—depleted mantle; CHUR—chondritic uniform reservoir. (**a**) $(^{176}Hf/^{177}Hf)/t(Ma)$; (**b**) $\varepsilon_{Hf}(t)/t(Ma)$.

5.3. Geodynamic Mechanism

The post-subduction magmas could share many of the geochemical and isotopic characteristics of the preceding arc magmatism [16,73,74]. The present zircon U-Pb ages of the Demingding monzogranites are dated at 17.3 ± 0.6 Ma (Figure 6a) and the rhyolites are dated at 186.5 ± 3 Ma (Figure 6b). These two age values should indicate two tectonic-magmatic events from oceanic subduction to continental collision. The ages of monzogranites are also consistent with those of most Miocene large to giant porphyry deposits in Gangdese under a similar tectonic setting [17,51,75], while the older ages of rhyolites show affinity with the oceanic subduction [76,77]. Significantly, recent studies suggested that the Neo-Tethyan subduction might have had an important influence on the large-scale magmatism and mineralization during this period [78].

Wang et al. [79] and Zhu et al. [23] have revealed that the south Lhasa terrane has undergone a transformation of tectonic regime, i.e., from ca. 250 Ma to 66 Ma. The Neo-Tethys oceanic plate continuously subducted northward, around the early stage (∼180 Ma), generating rhyolites and initial accumulation in the lower crust. At the same time, or later on, large-scale magmatic events may have been initiated by westward subduction of the ancient Pacific Ocean, which in turn led to triggering the remote effect of a tectonic transformation in the Tethys domain [76,78]. This is also supported by the late Yanshanian granites reported in the Duoba-Bange area, Gangdese belt, Tibet [80].

The early subduction of the Neo-Tethyan oceanic plate dragged the Indian plate lithosphere into the subduction zone, resulting in a continental collision between the Indian continent and the Eurasian continent, and the subduction of Neo-Tethys oceanic plate likely ceased at 65 Ma [81]. Then, there was upwelling of hot asthenosphere via a slab window, induced by the Neo-Tethys oceanic plate tearing [82]. Afterward, the Indian plate began under-thrusting to the north under the Lhasa terrane, resulting in the thickening of the south Lhasa terrane [83]. Continued upwelling of the asthenosphere resulted in delamination of the thickened lithosphere and the thinning of the subcontinental lithospheric mantle, causing the extension of the crust [84,85]. A large volume of fluids and melts were released, metasomatized the lithospheric mantle, and triggered partial melting, forming the initial mantle-derived magma [51,86].

At ca. 25∼11 Ma, the mantle-derived magmas underplated the accumulated thickened lower crust, forming H_2O-S-Cl(F)-rich alkaline melts [15]. Furthermore, the melts are compositionally similar to the andesite with high oxygen fugacity (fO_2) [81]. The andesite melts later preferentially mixed the Mo (Cu $\pm$ Au)-rich ancient crustal materials [74,87], evolved to Mo (Cu $\pm$ Au)-rich adakitic magmas, intruded into the prior Mid-Jurassic Yeba Formation (J_2y) as adakitic rocks, accompanied by pervasively extensive wall-rock alteration and ultimately formed the Demingding porphyry Mo (Cu) ore deposit (Figure 12).

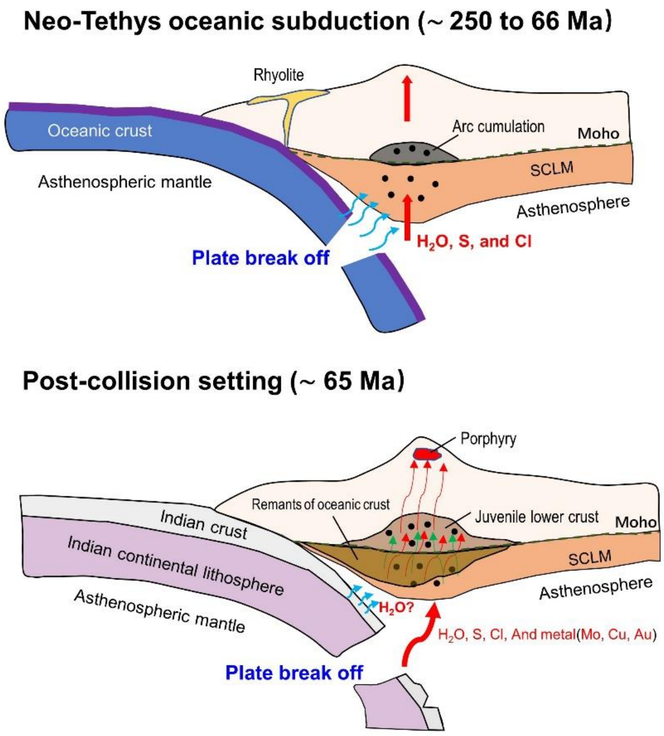

Figure 12. Schematic diagram showing the genetic and geodynamic model for the Miocene high-K felsic intrusion in Demingding porphyry Mo (Cu) deposit in Tibet.

6. Conclusions

On the basis of the geochronological data, whole-rock geochemical analysis, and in-situ U-Pb-Lu-Hf isotopes studies, we conclude as follows:

(1) Zircon U–Pb dating yielded crystallization age values of 17.3 $\pm$ 0.6 Ma and 186.5 $\pm$ 3.0 Ma for monzogranite and rhyolite in the Demingding deposit, respectively.
(2) The Demingding monzogranite is characterized by high- K calc-alkaline, adakitic affinities, and positive zircon ε_{Hf} (t) values (+0.9$\sim$+5.6, av.+3.1) with T_{DM2} (0.73–1.04 Ga). The rhyolite has similar ε_{Hf} (t) values of (+2.1$\sim$+7.3, av.+5.2) and T_{DM2} of (0.76–1.09 Ga) to those of monzogranites.
(3) Mo (Cu) ore-bodies produced in the monzogranite porphyry are the main ore types in this ore deposit, suggesting that Mo favors the silicate melt, as the confining pressure exerts a strong effect on the evolution of Mo concentration during fractional crystallization.
(4) The monzogranite is most probably derived from the remelting of the thickened lower crust. In addition, the ancient continental crust contributed to the formation of the porphyry Mo (Cu) deposit.

Author Contributions: Y.L. and K.D. conceived and designed the experiments; Y.L., H.Z. and Z.L. took part in the discussion; Y.L. and Z.L. took part in the field campaigns; Y.L. wrote the paper. All authors have read and agreed to the published version of the manuscript.

Funding: This research was financially funded by the Strategic Priority Research Program (B) of CAS (XDB18000000), the Natural Science Foundation of China (42073003), and the Guangxi Science and Technology Base and Talent Project (AD21220157).

Data Availability Statement: The data presented in this study are available on request from the corresponding authors.

Acknowledgments: This is a part of the Y.L postdoctoral project at University of Science and Technology of China. Special thanks go to Yilin Xiao (USTC) for his guidance and He Sun (HUST) and

Haiou Gu (HUST) for their great help during the study. This version significantly improved based on the four anonymous reviewer's great comments.

Conflicts of Interest: The authors declare no conflict of interest.

References

1. Mo, X.X.; Hou, Z.Q.; Niu, Y.L.; Dong, G.C.; Qu, X.M.; Zhao, Z.D.; Yang, Z.M. Mantle contributions to crustal thickening during continental collision: Evidence from Cenozoic igneous rocks in southern Tibet. *Lithos* **2007**, *96*, 225–242. [CrossRef]
2. Chung, S.L.; Lo, C.H.; Lee, T.Y.; Zhang, Y.; Xie, Y.; Li, X.; Wang, K.L.; Wang, P.L. The nature and timing of crustal thickening in Southern Tibet: Geochemical and zircon Hf isotopic constraints from postcollisional adakites. *Tectonophysics* **2009**, *477*, 36–48. [CrossRef]
3. Tang, J.X.; Zheng, W.B.; Chen, Y.C.; Wang, D.H.; Ying, L.J.; Qin, Z.P. Prospecting breakthrough of the deep porphyry ore body and its significance in Jiama copper polymetallic deposit, Tibet, China. *J. Jilin Univ.* **2013**, *43*, 1100–1110.
4. Hou, Z.Q.; Yang, Z.M.; Lu, Y.J.; Kemp, A.; Zheng, Y.C.; Li, Q.Y.; Tang, J.X.; Yang, Z.S.; Duan, L.F. A genetic linkage between subduction- and collision-related porphyry Cu deposits in continental collision zones. *Geology* **2015**, *43*, 247–250. [CrossRef]
5. Zheng, Y.F.; Mao, J.W.; Chen, Y.J.; Sun, W.D.; Ni, P.; Yang, X.Y. Hydrothermal ore deposits in collisional orogens. *Sci. Bull.* **2019**, *64*, 205–212. [CrossRef]
6. Cooke, D.R.; Hollings, P.; Walshe, J.L. Giant porphyry deposits: Characteristics, distribution, and tectonic controls. *Econ. Geol.* **2005**, *100*, 801–818. [CrossRef]
7. Sillitoe, R.H. Porphyry copper systems. *Econ. Geol.* **2010**, *105*, 3–41. [CrossRef]
8. Sun, W.D.; Huang, R.F.; Li, H.; Hu, Y.B.; Zhang, C.C.; Sun, S.J.; Zhang, L.P.; Ding, X.; Li, C.Y. Porphyry deposits and oxidized magmas. *Ore Geol. Rev.* **2015**, *65*, 97–131. [CrossRef]
9. Hou, Z.Q.; Cook, N.J. Metallogenesis of the Tibetan collisional orogen: A review and introduction to the special issue. *Ore Geol. Rev.* **2009**, *36*, 2–24. [CrossRef]
10. Chen, Y.J.; Pirajno, F.; Li, N.; Deng, X.H. The collision-type porphyry Mo deposits in Dabie Shan, China. *Ore Geol. Rev.* **2017**, *81*, 405–430. [CrossRef]
11. Sun, X.; Zheng, Y.Y.; Xu, J.; Huang, L.H.; Guo, F.; Gao, S.B. Metallogenesis and ore controls of Cenozoic porphyry Mo deposits in the Gangdese belt of southern Tibet. *Ore Geol. Rev.* **2017**, *81*, 996–1014. [CrossRef]
12. Lu, Y.G.; Xiao, Y.L.; Nadeau, O.; Yang, X.Y.; Wang, Y.Y.; Hou, Z.H.; Sun, H.; Li, D.Y.; Gu, H.O.; Deng, J.H. Inherited source affinity of Li and Hf isotopes for porphyry copper deposits from subduction and collisional settings. *Ore Geol. Rev.* **2021**, *138*, 104328. [CrossRef]
13. Sillitoe, R. Andean copper province: Tectonomagmatic settings, deposit types, metallogeny, exploration, and discovery. *Econ. Geol.* **2005**, *100*, 845–890.
14. Hou, Z.Q.; Gao, Y.F.; Qu, X.M.; Rui, Z.Y.; Mo, X.X. Origin of adakitic intrusives generated during mid-Miocene east–west extension in southern Tibet. *Earth Planet. Sci. Lett.* **2004**, *220*, 139–155. [CrossRef]
15. Hou, Z.Q.; Yang, Z.M.; Qu, X.M.; Meng, X.J.; Li, Z.Q.; Beaudoin, G.; Rui, Z.Y.; Gao, Y.F.; Zaw, K. The Miocene Gangdese porphyry copper belt generated during post-collisional extension in the Tibetan Orogen. *Ore Geol. Rev.* **2009**, *36*, 25–51. [CrossRef]
16. Richards, J.P. Postsubduction porphyry Cu-Au and epithermal Au deposits: Products of remelting of subduction-modified lithosphere. *Geology* **2009**, *37*, 247–250. [CrossRef]
17. Yang, Z.M.; Goldfarb, R.; Chang, Z.S. Generation of postcollisional porphyry copper deposits in southern Tibet triggered by subduction of the Indian continental plate. *Soc. Econ. Geol.* **2016**, *19*, 279–300.
18. Chung, S.L.; Liu, D.; Ji, J.; Chu, M.F.; Lee, H.Y.; Wen, D.J.; Lo, C.H.; Lee, T.Y.; Qian, Q.; Zhang, Q. Adakites from continental collision zones: Melting of thickened lower crust beneath southern Tibet. *Geology* **2003**, *31*, 1021–1024. [CrossRef]
19. Zheng, Y.C.; Hou, Z.Q.; Li, Q.Y.; Sun, Q.Z.; Liang, W.; Fu, Q.; Li, W.; Huang, K.X. Origin of Late Oligocene adakitic intrusives in the southeastern Lhasa terrane: Evidence from in situ zircon U–Pb dating, Hf–O isotopes, and whole-rock geochemistry. *Lithos* **2012**, *148*, 296–311. [CrossRef]
20. Zhang, Q.; Wang, Y.; Qing, Q.; Yang, J.H.; Wang, Y.L.; Zhao, T.P.; Guo, G.J. The characteristics and tectonic-metallogenic significances of the adakites in Yanshan period from eastern China. *Acta Petrol. Sin.* **2001**, *17*, 236–244.
21. Gao, S.; Rudnick, R.L.; Yuan, H.L.; Liu, X.M.; Liu, Y.S.; Xu, W.L.; Ling, W.L.; Ayers, J.; Wang, X.C.; Wang, Q.H. Recycling lower continental crust in the North China craton. *Nature* **2004**, *432*, 892–897. [CrossRef]
22. Sun, X.; Hollings, P.; Lu, Y.-J. Geology and origin of the Zhunuo porphyry copper deposit, Gangdese belt, southern Tibet. *Miner. Depos.* **2021**, *56*, 457–480. [CrossRef]
23. Zhu, D.C.; Wang, Q.; Zhao, Z.D.; Chung, S.L.; Cawood, P.A.; Niu, Y.L.; Liu, S.A.; Wu, F.Y.; Mo, X.X. Magmatic record of India-Asia collision. *Sci. Rep.* **2015**, *5*, 14289. [CrossRef]
24. Wang, B.D.; Xu, J.F.; Chen, J.L.; Zhang, X.G.; Wang, L.Q.; Xia, B.B. Petrogenesis and geochronology of the ore-bearing porphyritic rocks in Tangbula porphyry molybdenum-copper deposit in the eastern segment of the Gangdese metallogenic belt. *Acta Petrol. Sin.* **2010**, *26*, 1820–1832.

25. Zhang, Z.B.; Wang, L.Q.; Tang, P.; Lin, B.; Sun, M.; Qi, J.; Li, Y.X.; Yang, Z.K. Geochemistry and zircon trace elements composition of the Miocene ore©\bearing biotite monzogranite porphyry in the Demingding porphyry Cu-Mo deposit, Tibet: Petrogenesis and implication for magma fertility. *Geol. J.* **2020**, *55*, 4525–4542. [CrossRef]
26. Tang, P.; Tang, J.X.; Lin, B.; Wang, L.Q.; Zheng, W.B.; Leng, Q.F.; Gao, X.; Zhang, Z.B.; Tang, X.Q. Mineral chemistry of magmatic and hydrothermal biotites from the Bangpu porphyry Mo (Cu) deposit, Tibet. *Ore Geol. Rev.* **2019**, *115*, 103122. [CrossRef]
27. Allegre, C.O.; Courtillot, V.; Tapponnier, P.; Hirn, A.; Mattauer, M.; Coulon, C.; Jaeger, J.; Achache, J.; Schärer, U.; Marcoux, J. Structure and evolution of the Himalaya-Tibet orogenic belt. *Nature* **1984**, *307*, 17. [CrossRef]
28. Chung, S.L.; Lo, C.H.; Lee, T.Y.; Zhang, Y.; Xie, Y.; Li, X.; Wang, K.L.; Wang, P.L. Diachronous uplift of the Tibetan plateau starting 40? Myr ago. *Nature* **1998**, *394*, 769–773. [CrossRef]
29. Chung, S.L.; Wu, F.Y.; Zhao, Z.D. The Tibetan orogenic evolution: New advances from pre- to post-collisional geologic records. *J. Asian Earth Sci.* **2012**, *53*, 1–2. [CrossRef]
30. Yin, A.; Harrison, T.M. Geologic evolution of the Himalayan-Tibetan orogen. *Annu. Rev. Earth Planet. Sci.* **2000**, *28*, 211–280. [CrossRef]
31. Zhu, D.C.; Zhao, Z.D.; Pan, G.T.; Lee, H.Y.; Kang, Z.Q.; Liao, Z.L.; Wang, L.Q.; Li, G.M.; Dong, G.C.; Liu, B. Early cretaceous subduction-related adakite-like rocks of the Gangdese Belt, southern Tibet: Products of slab melting and subsequent melt-peridotite interaction? *J. Asian Earth Sci.* **2009**, *34*, 298–309. [CrossRef]
32. Zhu, D.C.; Zhao, Z.D.; Niu, Y.L.; Mo, X.X.; Chung, S.L.; Hou, Z.Q.; Wang, L.Q.; Wu, F.Y. The Lhasa Terrane: Record of a microcontinent and its histories of drift and growth. *Earth Planet. Sci. Lett.* **2011**, *301*, 241–255. [CrossRef]
33. Sun, X.; Lu, Y.J.; McCuaig, T.C.; Zheng, Y.Y.; Chang, H.F.; Guo, F.; Xu, L.J. Miocene ultrapotassic, high-Mg Dioritic, and adakite-like rocks from Zhunuo in Southern Tibet: Implications for mantle metasomatism and porphyry copper mineralization in collisional orogens. *J. Petrol.* **2018**, *59*, 341–386. [CrossRef]
34. Chen, Y.J.; Pirajno, F.; Li, N.; Deng, X.H. Molybdenum deposits in China. *Ore Geol. Rev.* **2017**, *81*, 401–404. [CrossRef]
35. Liu, X.Q.; Yan, J.; Wang, A.G.; Li, Q.Z.; Xie, J.C. Origin of the Cretaceous ore-bearing granitoids in the Beihuaiyang Zone, northern margin of the Dabie Orogen, Eastern China. *Int. Geol. Rev.* **2018**, *60*, 1453–1478. [CrossRef]
36. Hou, Z.; Wang, C. Determination of 35 trace elements in geological samples by inductively coupled plasma mass spectrometry. *J. Univ. Ence Technol. China* **2007**, *37*, 940–944.
37. Liu, Y.S.; Hu, Z.C.; Gao, S.; Günther, D.; Xu, J.; Gao, C.G.; Chen, H.H. In situ analysis of major and trace elements of anhydrous minerals by LA-ICP-MS without applying an internal standard. *Chem. Geol.* **2008**, *257*, 34–43. [CrossRef]
38. Chen, L.; Liu, Y.S.; Hu, Z.C.; Gao, S.; Zong, K.Q.; Chen, H.H. Accurate determinations of fifty-four major and trace elements in carbonate by LA–ICP-MS using normalization strategy of bulk components as 100%. *Chem. Geol.* **2011**, *284*, 283–295. [CrossRef]
39. Gu, H.-O.; Sun, H.; Wang, F.Y.; Ge, C.; Zhou, T.F. A new practical isobaric interference correction model for the in situ Hf isotopic analysis using laser ablation-multi-collector-ICP-mass spectrometry of zircons with high Yb/Hf ratios. *J. Anal. At. Spectrom.* **2019**, *34*, 1223–1232. [CrossRef]
40. Scherer, E.; Munker, C.; Mezger, K. Early Differentiation of the Crust-Mantle System: A Hf Isotope Perspective. *AGUFM* **2001**, *2001*, V52B-10.
41. Blichert-Toft, J.; Albarède, F. The Lu-Hf isotope geochemistry of chondrites and the evolution of the mantle-crust system. *Earth Planet. Sci. Lett.* **1997**, *148*, 243–258. [CrossRef]
42. Sun, S.S.; McDonough, W.F. Chemical and isotopic systematics of oceanic basalts: Implications for mantle composition and processes. *Geol. Soc. Lond. Spec. Publ.* **1989**, *42*, 313–345. [CrossRef]
43. Richards, J.P. Magmatic to hydrothermal metal fluxes in convergent and collided margins. *Ore Geol. Rev.* **2011**, *40*, 1–26. [CrossRef]
44. Richards, J.P.; Kerrich, R. Special paper: Adakite-like rocks: Their diverse origins and questionable role in metallogenesis. *Econ. Geol.* **2007**, *102*, 537–576. [CrossRef]
45. Defant, M.J.; Drummond, M.S. Derivation of some modern arc magmas by melting of young subducted lithosphere. *Nature* **1990**, *347*, 662–665. [CrossRef]
46. Guo, F.; Nakamuru, E.; Fan, W.M.; Kobayoshi, K.; Li, C.W. Generation of Palaeocene adakitic andesites by magma mixing; Yanji Area, NE China. *J. Petrol.* **2007**, *48*, 661–692. [CrossRef]
47. Yang, Z.M.; Hou, Z.Q.; White, N.C.; Chang, Z.S.; Li, Z.Q.; Song, Y.C. Geology of the post-collisional porphyry copper-molybdenum deposit at Qulong, Tibet. *Ore Geol. Rev.* **2009**, *36*, 133–159. [CrossRef]
48. Zheng, Y.Y.; Sun, X.; Gao, S.B.; Zhao, Z.D.; Zhang, G.Y.; Wu, S.; You, Z.M.; Li, J.D. Multiple mineralization events at the Jiru porphyry copper deposit, southern Tibet: Implications for Eocene and Miocene magma sources and resource potential. *J. Asian Earth Sci.* **2014**, *79*, 842–857. [CrossRef]
49. Mahéo, G.; Guillot, S.; Blichert-Toft, J.; Rolland, Y.; Pêcher, A. A slab breakoff model for the Neogene thermal evolution of South Karakorum and South Tibet. *Earth Planet. Sci. Lett.* **2002**, *195*, 45–58. [CrossRef]
50. Martin, H.; Smithies, R.H.; Rapp, R.; Moyen, J.F.; Champion, D. An overview of adakite, tonalite–trondhjemite–granodiorite (TTG), and sanukitoid: Relationships and some implications for crustal evolution. *Lithos* **2005**, *79*, 1–24. [CrossRef]
51. Hou, Z.Q.; Duan, L.F.; Lu, Y.J.; Zheng, Y.C.; Zhu, D.C.; Yang, Z.M.; Yang, Z.S.; Wang, B.D.; Pei, Y.R.; Zhao, Z.; et al. Lithospheric architecture of the Lhasa terrane and its control on ore deposits in the Himalayan-Tibetan orogen. *Econ. Geol.* **2015**, *110*, 1541–1575. [CrossRef]

52. Guo, Z.F.; Wilson, M.; Liu, J.Q. Post-collisional adakites in south Tibet: Products of partial melting of subduction-modified lower crust. *Lithos* **2007**, *96*, 205–224. [CrossRef]
53. Ji, W.Q.; Wu, F.Y.; Chung, S.L.; Li, J.X.; Liu, C.Z. Zircon U–Pb geochronology and Hf isotopic constraints on petrogenesis of the Gangdese batholith, southern Tibet. *Chem. Geol.* **2009**, *262*, 229–245. [CrossRef]
54. Castillo, P.R. Adakite petrogenesis. *Lithos* **2012**, *134*, 304–316. [CrossRef]
55. Xu, W.C.; Zhang, H.F.; Guo, L.; Yuan, H.L. Miocene high Sr/Y magmatism, south Tibet: Product of partial melting of subducted Indian continental crust and its tectonic implication. *Lithos* **2010**, *114*, 293–306. [CrossRef]
56. Chen, J.L.; Xu, J.F.; Yu, H.X.; Wang, B.D.; Wu, J.B.; Feng, Y.X. Late Cretaceous high-Mg# granitoids in southern Tibet: Implications for the early crustal thickening and tectonic evolution of the Tibetan Plateau? *Lithos* **2015**, *232*, 12–22.
57. Tang, M.; Lee, C.T.; Ji, W.Q.; Wang, R.; Costin, G. Crustal thickening and endogenic oxidation of magmatic sulfur. *Sci. Adv.* **2020**, *6*, eaba6342. [CrossRef]
58. Allègre, C.J.; Minster, J.F. Quantitative models of trace element behavior in magmatic processes. *Earth Planet. Sci. Lett.* **1978**, *38*, 1–25. [CrossRef]
59. Yang, Z.M.; Hou, Z.Q.; Chang, Z.S.; Li, Q.Y.; Liu, Y.F.; Qu, H.C.; Sun, M.Y.; Xu, B. Cospatial Eocene and Miocene granitoids from the Jiru Cu deposit in Tibet: Petrogenesis and implications for the formation of collisional and postcollisional porphyry Cu systems in continental collision zones. *Lithos* **2016**, *245*, 243–257. [CrossRef]
60. Streck, M.J.; Leeman, W.P.; Chesley, J.T. High-magnesian andesite from Mount Shasta: A product of magma mixing and contamination, not a primitive melt: COMMENT AND REPLY: REPLY. *Geology* **2007**, *35*, e148. [CrossRef]
61. Yang, Z.; Hou, Z. Porphyry Cu deposits in collisional orogen setting: A preliminary genetic model. *Miner. Depos.* **2009**, *28*, 515–538.
62. Zou, B.; Lin, B.; Zheng, W.B.; Song, Y.; Tang, P.; Zhang, Z.B.; Xin, G. The characteristics of alteration and mineralization and geochronology of ore-bearing porphyry in south pit of Jiama copper-polymetallic deposit, Tibet. *Acta Petrol. Sin.* **2019**, *35*, 953–967.
63. Liu, S.A.; Li, S.G.; He, Y.S.; Huang, F. Geochemical contrasts between early Cretaceous ore-bearing and ore-barren high-Mg adakites in central-eastern China: Implications for petrogenesis and Cu—Au mineralization. *Geochim. Cosmochim. Acta* **2010**, *74*, 7160–7178. [CrossRef]
64. Guan, Q.; Zhu, D.C.; Zhao, Z.D.; Dong, G.C.; Zhang, L.L.; Li, X.W.; Liu, M.; Mo, X.X.; Liu, Y.S.; Yuan, H.L. Crustal thickening prior to 38Ma in southern Tibet: Evidence from lower crust-derived adakitic magmatism in the Gangdese Batholith. *Gondwana Res.* **2012**, *21*, 88–99. [CrossRef]
65. Lee, C.T.A.; Tang, M. How to make porphyry copper deposits. *Earth Planet. Sci. Lett.* **2020**, *529*, 115868. [CrossRef]
66. Rapp, R.P.; Shimizu, N.; Norman, M.D.; Applegate, G.S. Reaction between slab-derived melts and peridotite in the mantle wedge: Experimental constraints at 3.8 GPa. *Chem. Geol.* **1999**, *160*, 335–356. [CrossRef]
67. Wang, Q.; Wyman, D.A.; Xu, J.F.; Zhao, Z.H.; Jian, P.; Zi, F. Partial Melting of Thickened or Delaminated Lower Crust in the Middle of Eastern China: Implications for Cu-Au Mineralization. *J. Geol.* **2007**, *115*, 149–161. [CrossRef]
68. Hu, Y.B.; Liu, J.Q.; Ling, M.X.; Liu, Y.; Ding, X.; Liu, D.Y.; Sun, W.D. Constraints on the origin of adakites and porphyry Cu-Mo mineralization in Chongjiang, Southern Gangdese, the Tibetan Plateau. *Lithos* **2017**, *292–293*, 424–436. [CrossRef]
69. Xiao, L.; Clemens, J.D. Origin of potassic (C-type) adakite magmas: Experimental and field constraints. *Lithos* **2007**, *95*, 399–414. [CrossRef]
70. White, W.; Bookstrom, A.; Kamilli, R.; Ganster, M.; Smith, R.; Ranta, D.; Steininger, R. Character and origin of Climax-type molybdenum deposits. *Econ. Geol.* **1981**, *75*, 270–316.
71. Farmer, G.L.; DePaolo, D.J. Origin of Mesozoic and Tertiary granite in the western United States and implications for Pre-Mesozoic crustal structure: 1. Nd and Sr isotopic studies in the geocline of the Northern Great Basin. *J. Geophys. Res. Solid Earth* **1983**, *88*, 3379–3401. [CrossRef]
72. Klemm, L.M.; Pettke, T.; Heinrich, C.A.; Campos, E. Hydrothermal evolution of the El Teniente deposit, Chile: Porphyry Cu-Mo ore deposition from low-salinity magmatic fluids. *Econ. Geol.* **2007**, *102*, 1021–1045. [CrossRef]
73. Chen, J.L.; Xu, J.F.; Wang, B.D.; Yang, Z.M.; Ren, J.B.; Yu, H.X.; Liu, H.F.; Feng, Y.X. Geochemical differences between subduction- and collision-related copper-bearing porphyries and implications for metallogenesis. *Ore Geol. Rev.* **2015**, *70*, 424–437. [CrossRef]
74. Xu, J.; Zheng, Y.Y.; Sun, X.; Shen, Y.H. Geochronology and petrogenesis of Miocene granitic intrusions related to the Zhibula Cu skarn deposit in the Gangdese belt, southern Tibet. *J. Asian Earth Sci.* **2016**, *120*, 100–116. [CrossRef]
75. Zeng, Y.C.; Chen, J.L.; Xu, J.F.; Lei, M.; Xiong, Q.W. Origin of Miocene Cu-bearing porphyries in the Zhunuo region of the southern Lhasa subterrane: Constraints from geochronology and geochemistry. *Gondwana Res.* **2017**, *41*, 51–64. [CrossRef]
76. Deng, J.H.; Yang, X.Y.; Zartman, R.E.; Qi, H.S.; Zhang, L.P.; Liu, H.; Zhang, Z.F.; Mastoi, A.S.; Al Emil, G.B.; Sun, W.D. Early cretaceous transformation from Pacific to Neo-Tethys subduction in the SW Pacific Ocean: Constraints from Pb-Sr-Nd-Hf isotopes of the Philippine arc. *Geochim. Cosmochim. Acta* **2020**, *285*, 21–40. [CrossRef]
77. Deng, J.H.; Yang, X.Y.; Qi, H.S.; Zhang, Z.F.; Mastoi, A.S.; Al Emil, G.B.; Sun, W.D. Early Cretaceous adakite from the Atlas porphyry Cu-Au deposit in Cebu Island, Central Philippines: Partial melting of subducted oceanic crust. *Ore Geol. Rev.* **2019**, *110*, 102937. [CrossRef]
78. Sun, W.D. Initiation and evolution of the South China Sea: An overview. *Chin. J. Geochem.* **2016**, *35*, 215–225.

79. Wang, R.; Richards, J.P.; Hou, Z.Q.; Yang, Z.M.; DuFrane, S.A. Increased Magmatic Water Content—The Key to Oligo-Miocene Porphyry Cu-Mo ± Au Formation in the Eastern Gangdese Belt, Tibet. *Econ. Geol.* **2014**, *109*, 1315–1339. [CrossRef]
80. Zhang, J.C.; Wang, X.W.; Lei, C.Y.; Peng, H.I.; Hu, Z.L. Genesis of late Yanshanian granites and the ore-search prospect in the Duoba-Bange area, Gangdise Belt, Tibet, China. *J. Chengdu Univ. Technol.* **2011**, *38*, 671–677.
81. Hou, Z.Q.; Zheng, Y.C.; Yang, Z.M.; Rui, Z.Y.; Zhao, Z.D.; Jiang, S.H.; Qu, X.M.; Sun, Q.Z. Contribution of mantle components within juvenile lower-crust to collisional zone porphyry Cu systems in Tibet. *Miner. Depos.* **2013**, *48*, 173–192. [CrossRef]
82. Zhao, X.Y.; Yang, Z.S.; Zheng, Y.C.; Liu, Y.C.; Tian, S.; Fu, Q. Geology and genesis of the post-collisional porphyry–skarn deposit at Bangpu, Tibet. *Ore Geol. Rev.* **2015**, *70*, 486–509. [CrossRef]
83. Ji, W.Q.; Wu, F.Y.; Liu, C.Z.; Chung, S.L. Early Eocene crustal thickening in southern Tibet: New age and geochemical constraints from the Gangdese batholith. *J. Asian Earth Sci.* **2012**, *53*, 82–95. [CrossRef]
84. Mo, X.X.; Niu, Y.L.; Dong, G.C.; Zhao, Z.D.; Hou, Z.Q.; Zhou, S.; Ke, S. Contribution of syncollisional felsic magmatism to continental crust growth: A case study of the Paleogene Linzizong volcanic Succession in southern Tibet. *Chem. Geol.* **2008**, *250*, 49–67. [CrossRef]
85. Liu, D.; Zhao, Z.D.; DePaolo, D.J.; Zhu, D.C.; Meng, F.Y.; Shi, Q.S.; Wang, Q. Potassic volcanic rocks and adakitic intrusions in southern Tibet: Insights into mantle–crust interaction and mass transfer from Indian plate. *Lithos* **2017**, *268*, 48–64. [CrossRef]
86. Liu, D.; Zhao, Z.D.; Zhu, D.C.; Niu, Y.L.; DePaolo, D.J.; Harrison, T.M.; Mo, X.X.; Dong, G.; Zhou, S.; Sun, C. Postcollisional potassic and ultrapotassic rocks in southern Tibet: Mantle and crustal origins in response to India–Asia collision and convergence. *Geochim. Cosmochim. Acta* **2014**, *143*, 207–231. [CrossRef]
87. Li, Y.L.; Li, X.H.; Wang, C.S.; Wei, Y.S.; Chen, X.; He, J.; Xu, M.; Hou, Y.L. Miocene adakitic intrusions in the Zhongba terrane: Implications for the origin and geochemical variations of post-collisional adakitic rocks in southern Tibet. *Gondwana Res.* **2017**, *41*, 65–76. [CrossRef]